



# The Study of the Physical Properties and Energy Sources of Five Luminous Type Ibc Supernovae

Song-Yao Bai (白松瑶)<sup>1</sup>, Tao Wang (王涛)<sup>1</sup>, Shan-Qin Wang (王善钦)<sup>1</sup>, Wen-Pei Gan (甘文沛)<sup>2</sup>, Liu-Yi Wang (王浏毅)<sup>1</sup>, and En-Wei Liang (梁恩维)<sup>1</sup>

<sup>1</sup> Guangxi Key Laboratory for Relativistic Astrophysics, School of Physical Science and Technology, Guangxi University, Nanning 530004, China  
[shanqinwang@gxu.edu.cn](mailto:shanqinwang@gxu.edu.cn)

<sup>2</sup> Nanjing Institute of Astronomical Optics & Technology, Nanjing 210042, China

Received 2023 June 12; revised 2023 August 7; accepted 2023 August 30; published 2023 October 25

## Abstract

In this paper, we study five luminous supernovae (LSNe) Ibc (SN 2009ca, ASASSN-15mj, SN 2019omd, SN 2002ued, and SN 2021bmf) whose peak absolute magnitudes  $M_{\text{peak}}$  are  $\approx -19.5$  to  $-21$  mag by fitting their multi-band light curves (LCs) with different energy source models. We find that SN 2009ca might be powered by the  $^{56}\text{Ni}$  model since the required  $^{56}\text{Ni}$  mass ( $0.56 M_{\odot}$ ) is comparable to those of energetic SNe Ic, while the rest four SNe cannot be accounted for the  $^{56}\text{Ni}$  model since their derived  $^{56}\text{Ni}$  masses are  $\gtrsim 1 M_{\odot}$  or the ratios of the  $^{56}\text{Ni}$  mass to the ejecta mass are larger than 0.2. This indicates that some LSNe might be powered by  $^{56}\text{Ni}$  decay, while most of them need additional energy sources. We then use the magnetar plus  $^{56}\text{Ni}$  model and the fallback plus  $^{56}\text{Ni}$  model to fit the LCs of the four LSNe that cannot be explained by the  $^{56}\text{Ni}$  model, finding that the two models can account for the four SNe, and the derived parameters are comparable to those of LSNe or superluminous SNe in the literature, if they were (mainly) powered by magnetars or fallback. We suggest that the magnetar plus  $^{56}\text{Ni}$  model is more reasonable than the fallback plus  $^{56}\text{Ni}$  model, since the validity of the fallback plus  $^{56}\text{Ni}$  model depends on the value of accretion efficiency ( $\eta$ ) and favors a large  $\eta$  value, and the magnetar plus  $^{56}\text{Ni}$  model yields smaller  $\chi^2/\text{dof}$  values. It should be pointed out that, however, the fallback plus  $^{56}\text{Ni}$  model is still a promising model that can account for the four SNe in our sample as well as other LSNe.

*Key words:* Stars – (stars:) supernovae: general – stars: magnetars

## 1. Introduction

Core-collapse supernovae (CCSNe) result from the explosions of massive stars with zero-age main-sequence mass ( $M_{\text{ZAMS}} \gtrsim 8.0 M_{\odot}$ ) (Woosley et al. 2002; Janka et al. 2007). It is believed that the progenitors losing most or all hydrogen envelopes can produce stripped-envelope SNe (SESNe) which can be divided into type IIb SNe, type Ib SNe, and type Ic SNe (see Filippenko 1997; Gal-Yam 2017 for reviews), for which the progenitors lost most hydrogen envelopes, all hydrogen envelopes, and most helium envelopes, respectively.

Most types Ib and Ic (type Ibc) SNe are dimmer than type Ia SNe whose peak absolute magnitudes  $M_{\text{peak}}$  are  $\sim -19.5$  mag. Over the past two decades, however, a few hundred superluminous type Ibc SNe (SLSNe Ibc) with  $M_{\text{peak}} \lesssim -21$  mag were confirmed and comprehensively studied (see Gal-Yam 2012 and Gal-Yam 2019 for reviews). Additionally, a few dozen luminous type Ibc SNe (LSNe Ibc) whose  $M_{\text{peak}}$  are between  $\sim -19.5$  and  $\sim -21$  mag are also been studied.<sup>3</sup>

Unlike normal type Ibc which is believed to be (mainly) powered by the cascade decay of  $^{56}\text{Ni}$  synthesized by the explosions (Colgate & McKee 1969; Colgate et al. 1980; Arnett 1982), the energy sources of LSNe Ibc and SLSNe Ibc are still elusive.

Previous studies for SLSNe Ibc indicate that almost all SLSNe cannot be explained by the  $^{56}\text{Ni}$  model (including the pair-instability SNe model which need a few  $M_{\odot}$  of  $^{56}\text{Ni}$ ). To account for the light curves (LCs) of SLSNe which cannot be explained by the  $^{56}\text{Ni}$  model, three models which are the magnetar model (Maeda et al. 2007; Kasen & Bildsten 2010; Woosley 2010; Inserra et al. 2013; Wang et al. 2015a), the SN ejecta-circumstellar medium (CSM) interaction (CSI) model (Chevalier 1982; Chevalier & Fransson 1994; Chatzopoulos et al. 2012, 2013), and the fallback accretion model (hereafter the fallback model; Dexter & Kasen 2013; Moriya et al. 2018a, 2018b; Anderson et al. 2018; Li et al. 2020) have been proposed.

The case for LSNe Ibc is more complicated. Wang et al. (2015b) suggest that the magnetar plus  $^{56}\text{Ni}$  model is a promising model to account for LSNe Ic since the  $^{56}\text{Ni}$  masses needed by the  $^{56}\text{Ni}$  model are larger than the reasonable values,

<sup>3</sup> Richardson et al. (2002) show that  $M_{\text{peak,B}}$  of SNe Ia are  $\sim -19.5$  mag, while Gal-Yam (2012) suggests that the threshold of SLSNe is  $-21$  mag. Therefore, Wang et al. (2015b) suggest that the SNe with  $M_{\text{peak}}$  in  $-19.5$  to  $-21$  mag are LSNe.

**Table 1**  
The Information on Five Luminous Supernovae

Name	R.A. (J2000)	Decl. (J2000)	Type	Redshift	$M_{\text{rest,peak}}$ (mag)	References <sup>a</sup>
SN 2009ca	21 <sup>h</sup> 26 <sup>m</sup> 22 <sup>s</sup> .20	−40°2′48″.6	Ic-BL	0.096	$r = -19.77$	1,2
ASASSN-15mj	14 <sup>h</sup> 02 <sup>m</sup> 15 <sup>s</sup> .64	+33°2′40″.29	Ib	0.034	$V = -19.5$	3
SN 2019omd	00 <sup>h</sup> 36 <sup>m</sup> 57 <sup>s</sup> .972	−03°2′39″.17	Ib	0.082	$r = -19.76$	4
SN 2021bmf	16 <sup>h</sup> 33 <sup>m</sup> 29 <sup>s</sup> .408	−06°2′49″.58	Ic-BL	0.04	$r = -20.4$	4
SN 2022ued	08 <sup>h</sup> 54 <sup>m</sup> 45 <sup>s</sup> .854	+78°2′48″.43	Ib	0.1087	$r = -20.5$	4

**Note.**

<sup>a</sup> References. (1) Taddia et al. (2018); (2) Stritzinger et al. (2018); (3) Shappee et al. (2014); (4) <https://sites.astro.caltech.edu/ztf/bts> (Perley et al. 2020).

while the contribution of a moderate amount of  $^{56}\text{Ni}$  cannot be neglected. Wang et al. (2015b) use the magnetar plus  $^{56}\text{Ni}$  model to fit the bolometric LCs of three LSNe Ic-BL (SN 2010ay, SN 2006nx, and SN 14475), and find that the model can explain their LCs and the derived parameters for magnetar were  $P_0 \sim 7\text{--}15$  ms and  $B \sim (4\text{--}7) \times 10^{14}$  G. Gomez et al. (2021) investigated SN 2019stc and found that the first and second peaks in this SN could be powered by the magnetar plus  $^{56}\text{Ni}$  decay and the ejecta-CSM interaction, respectively. Gomez et al. (2022) used the magnetar plus  $^{56}\text{Ni}$  model to fit the multi-band LCs of 40 LSNe with  $r$  band  $M_{\text{peak}}$  between  $-19\text{mag}$  and  $-20\text{mag}$ , finding that the parameters of magnetars were  $P_0 \sim 1\text{--}23$  ms and  $B \sim (0.1\text{--}13) \times 10^{14}$  G.

In this paper, we collect the multi-band data of five LSNe Ib with  $M_{\text{peak}} \approx -19.5$  to  $-21\text{mag}$ , and constrain their physical properties by using the  $^{56}\text{Ni}$  model, the magnetar plus  $^{56}\text{Ni}$  model, as well as the fallback plus  $^{56}\text{Ni}$  model to fit their multi-band LCs. In Section 2, we model the multi-band LCs of the five LSNe using these three models. In Section 3, we discuss our results and draw some conclusions in Section 4. Throughout the paper, we assume  $\Omega_m = 0.315$ ,  $\Omega_\Lambda = 0.685$ , and  $H_0 = 67.3 \text{ km s}^{-1} \text{ Mpc}^{-1}$  (Planck Collaboration et al. 2014). The values of the Milky Way reddening ( $E_{B-V}$ ) of all events are from Schlafly & Finkbeiner (2011).

## 2. Modeling the Multi-band Light Curves of Five LSNe

We collect about 50 LSNe Ib with  $M_{\text{peak}} \approx -19.5$  to  $-21\text{mag}$  from the Open Supernova Catalog (Guillochon et al. 2017)<sup>4</sup> and the public catalog of transients from the Zwicky Transient Facility (ZTF) Bright Transient Survey (BTS) (Perley et al. 2020).<sup>5</sup> We then exclude the LSNe which had been fitted by the literature (e.g., Wang et al. 2015b; Gomez et al. 2021, 2022), and obtain the rest five LSNe, which are SN 2009ca, ASASSN-15mj, SN 2019omd, SN 2021bmf, and SN 2022ued. Among the five LSNe, ASASSN-15mj, SN 2019omd, and

SN 2022ued are SNe Ib, while SN 2009ca and SN 2021bmf are broad-lined SNe Ic (SNe Ic-BL). The information of the five LSNe is listed in Table 1.

### 2.1. Modeling the Multi-band LCs of Five LSNe Using the $^{56}\text{Ni}$ Model

We first use the  $^{56}\text{Ni}$  model to fit the multi-band light curves (LCs) of the five SNe in our sample. The details of the  $^{56}\text{Ni}$  model can be found in Wang et al. (2023) and references therein. Throughout this paper,  $\kappa$  is set to be  $0.07 \text{ cm}^2 \text{ g}^{-1}$ . Definitions, units, and prior ranges of the free parameters of the  $^{56}\text{Ni}$  model are listed in Table 2. We use the Markov Chain Monte Carlo (MCMC) method to derive the medians and  $1\sigma$  confidence regions of the parameters through the emcee Python package (Foreman-Mackey et al. 2013).

The fits for the five SNe using the  $^{56}\text{Ni}$  model are shown in Figure 1. The parameters and the corresponding corner plots are presented in Table 3 and Figures A1–A5.

Based on the derived  $M_{\text{ej}}$  and  $v_{\text{ph}}$ , we can calculate the values of  $E_K$  of the SNe ( $E_K = 0.3M_{\text{ej}}v_{\text{ph}}^2$ ). We find that  $E_K$  of SN 2009ca, ASASSN-15mj, SN 2019omd, SN 2021bmf, and SN 2022ued are  $1.53 \times 10^{52}$  erg,  $1.62 \times 10^{51}$  erg,  $4.82 \times 10^{51}$  erg,  $2.31 \times 10^{52}$  erg, and  $5.57 \times 10^{51}$  erg, respectively.

The derived values of  $M_{\text{ej}}$ ,  $M_{\text{Ni}}$ ,  $v_{\text{ph}}$ , and  $E_K$  are  $\sim (0.7\text{--}8.0) M_\odot$ ,  $\sim (0.7\text{--}5.0) M_\odot$ ,  $\sim (1.0\text{--}2.5) \times 10^9 \text{ cm s}^{-1}$ , and  $\sim (1.0\text{--}25.0) \times 10^{51}$  erg, respectively; the mean values of these parameters are  $\sim 5.45 M_\odot$ ,  $\sim 2.79 M_\odot$ ,  $\sim 1.73 \times 10^9 \text{ cm s}^{-1}$ , and  $\sim 10.0 \times 10^{51}$  erg, respectively. The ratios of  $M_{\text{Ni}}$  to  $M_{\text{ej}}$  ( $f$ ) of the five SNe are  $\sim 0.22\text{--}0.99$ .

By comparing our derived parameters to those in the literature, we find that the values of derived  $M_{\text{Ni}}$  and  $f$  of the  $^{56}\text{Ni}$  model are consistent with those derived from other LSNe using the  $^{56}\text{Ni}$  model, which are  $\sim (1.0\text{--}2.0) M_\odot$  and  $0.31\text{--}0.62$  (Wang et al. 2015b) or  $\approx 3.2 M_\odot$  and  $\sim 0.31$  (Gomez et al. 2021).

As pointed out by Khatami & Kasen (2019) and Arnett (1982), Afsariardchi et al. (2021)'s model might overestimate the  $^{56}\text{Ni}$  masses of SNe. More reasonable  $^{56}\text{Ni}$  masses can be

<sup>4</sup> <https://sne.space>

<sup>5</sup> <https://sites.astro.caltech.edu/ztf/bts/bts.php>

**Table 2**  
Definitions, Units, and Prior Ranges of the Parameters of the  $^{56}\text{Ni}$  model<sup>a</sup>

Parameter	Definition	Unit	Prior
$^{56}\text{Ni}$ modles			
$M_{\text{ej}}$	The ejecta mass	$M_{\odot}$	[0.1, 50]
$v_{\text{ph}}$	The early-time photospheric velocity	$10^9 \text{ cm s}^{-1}$	[0.1, 5]
$M_{\text{Ni}}$	The $^{56}\text{Ni}$ mass	$M_{\odot}$	[0.0, 5]
$\log \kappa_{\gamma, \text{Ni}}$	The $\gamma$ -ray opacity of $^{56}\text{Ni}$ -cascade-decay photons	$\text{cm}^2 \text{ g}^{-1}$	[-1.568, 4]
$T_{\text{f}}$	The temperature floor of the photosphere	K	[1000, $10^4$ ]
$t_{\text{shift}}$	The explosion time relative to the first data	day	[-20, 0]
$A_{\text{host,V}}$	The extinction in the host galaxy	mag	[0, 1]
$\lambda_{\text{CF}}$	The cutoff wavelength	$\text{\AA}$	[0, 4000]
$\beta'$	The dimensionless free parameter		[0, 10]
$\chi^2/\text{dof}$			

**Note.**

<sup>a</sup> For SNe without UV photometric data,  $\lambda_{\text{CF}}$  and  $\beta'$  are set to be  $3000 \text{ \AA}$  and 1, respectively.

**Table 3**  
Medians,  $1\sigma$  Bounds, and Best-fitting Values (in Parentheses) of the Parameters of the  $^{56}\text{Ni}$  Model

Parameter	SN 2009ca	ASASSN-15mj	SN 2019omd	SN 2021bmf	SN 2022ued
$^{56}\text{Ni}$ modle					
$M_{\text{ej}}(M_{\odot})$	$5.78^{+0.14}_{-0.13}$ (5.82)	$0.84^{+0.09}_{-0.09}$ (0.79)	$7.78^{+1.39}_{-1.25}$ (8.02)	$7.03^{+0.89}_{-0.85}$ (6.35)	$6.34^{+0.29}_{-1.20}$ (6.26)
$v_{\text{ph}}(10^9 \text{ cm s}^{-1})$	$2.10^{+0.03}_{-0.03}$ (2.10)	$1.99^{+0.29}_{-0.20}$ (1.85)	$1.01^{+0.05}_{-0.05}$ (1.00)	$2.52^{+0.17}_{-0.15}$ (2.47)	$1.25^{+0.05}_{-0.04}$ (1.22)
$M_{\text{Ni}}(M_{\odot})$	$1.26^{+0.01}_{-0.01}$ (1.26)	$0.79^{+0.08}_{-0.07}$ (0.78)	$2.26^{+0.20}_{-0.13}$ (2.14)	$4.36^{+0.45}_{-0.68}$ (4.77)	$4.98^{+0.01}_{-0.06}$ (4.99)
$\log \kappa_{\gamma, \text{Ni}}(\text{cm}^2 \text{ g}^{-1})$	$-1.30^{+0.02}_{-0.02}$ (-1.30)	$-1.34^{+0.22}_{-0.16}$ (-1.40)	$1.29^{+1.85}_{-1.84}$ (-0.34)	$-1.48^{+0.06}_{-0.06}$ (-1.46)	$-1.42^{+2.35}_{-0.04}$ (-1.45)
$T_{\text{f}}(\text{K})$	$6239.02^{+29.00}_{-24.43}$ (6233.46)	$2957.43^{+1345.78}_{-1333.03}$ (3437.09)	$2380.15^{+938.14}_{-942.07}$ (1857.71)	$6173.63^{+324.56}_{-383.72}$ (6429.65)	$2079.51^{+330.47}_{-389.53}$ (2207.24)
$t_{\text{shift}}(\text{day})$	$-19.93^{+0.12}_{-0.06}$ (-19.96)	$-9.95^{+1.37}_{-1.25}$ (-10.18)	$-15.11^{+1.24}_{-1.38}$ (-15.00)	$-9.32^{+0.63}_{-0.63}$ (-9.36)	$-18.22^{+1.26}_{-1.50}$ (-18.95)
$A_{\text{host,V}}(\text{mag})$	$0.00^{+0.01}_{-0.00}$ (0.00)	$0.03^{+0.04}_{-0.02}$ (0.01)	$0.10^{+0.10}_{-0.07}$ (0.04)	$0.37^{+0.09}_{-0.16}$ (0.45)	$0.00^{+0.00}_{-0.00}$ (0.00)
$\lambda_{\text{CF}}(\text{\AA})$	$3625.28^{+227.09}_{-145.34}$ (3622.56)	$3370.75^{+52.11}_{-82.89}$ (3398.80)	...	...	...
$\beta'$	$5.22^{+2.81}_{-1.81}$ (5.13)	$1.37^{+0.19}_{-0.18}$ (1.52)	...	...	...
$\chi^2/\text{dof}$	22.71 (22.69)	1.83 (1.69)	0.47 (0.45)	2.97 (2.95)	8.80 (8.65)

**Note.** The values of  $\chi^2/\text{dof}$  (reduced  $\chi^2$ , dof = degree of freedom) are also presented.

derived by using the equation (Khatami & Kasen 2019)

$$M_{\text{Ni}} = \frac{L_{\text{p}} \beta^2 t_{\text{p}}^2}{2 \epsilon_{\text{Ni}} \tau_{\text{Ni}}^2} \left( \left( 1 - \frac{\epsilon_{\text{Co}}}{\epsilon_{\text{Ni}}} \right) \times (1 - (1 + \beta t_{\text{p}} / \tau_{\text{Ni}}) e^{-\beta t_{\text{p}} / \tau_{\text{Ni}}}) + \frac{\epsilon_{\text{Co}} \tau_{\text{Co}}^2}{\epsilon_{\text{Ni}} \tau_{\text{Ni}}^2} (1 - (1 + \beta t_{\text{p}} / \tau_{\text{Co}}) e^{-\beta t_{\text{p}} / \tau_{\text{Co}}}) \right)^{-1}, \quad (1)$$

the mean values of  $\beta$  for Type Ib and Type Ic-BL SNe are 0.66 and 0.56, respectively (Afsariardchi et al. 2021); the rise time  $t_{\text{p}}$  and the peak luminosity  $L_{\text{p}}$  are given by the bolometric LC reproduced by the best-fitting parameters of multi-band LCs fits. Using the equation, the  $^{56}\text{Ni}$  masses of the five SNe are  $0.56 M_{\odot}$ ,  $0.44 M_{\odot}$ ,  $0.99 M_{\odot}$ ,  $2.26 M_{\odot}$ , and  $2.28 M_{\odot}$ , respectively. The values of  $f$  are  $\sim 0.10$  (SN 2009ca),  $\sim 0.56$  (ASASSN-15mj),  $\sim 0.12$  (SN 2019omd),  $\sim 0.36$  (SN 2021bmf), and  $\sim 0.36$  (SN 2022ued), respectively.

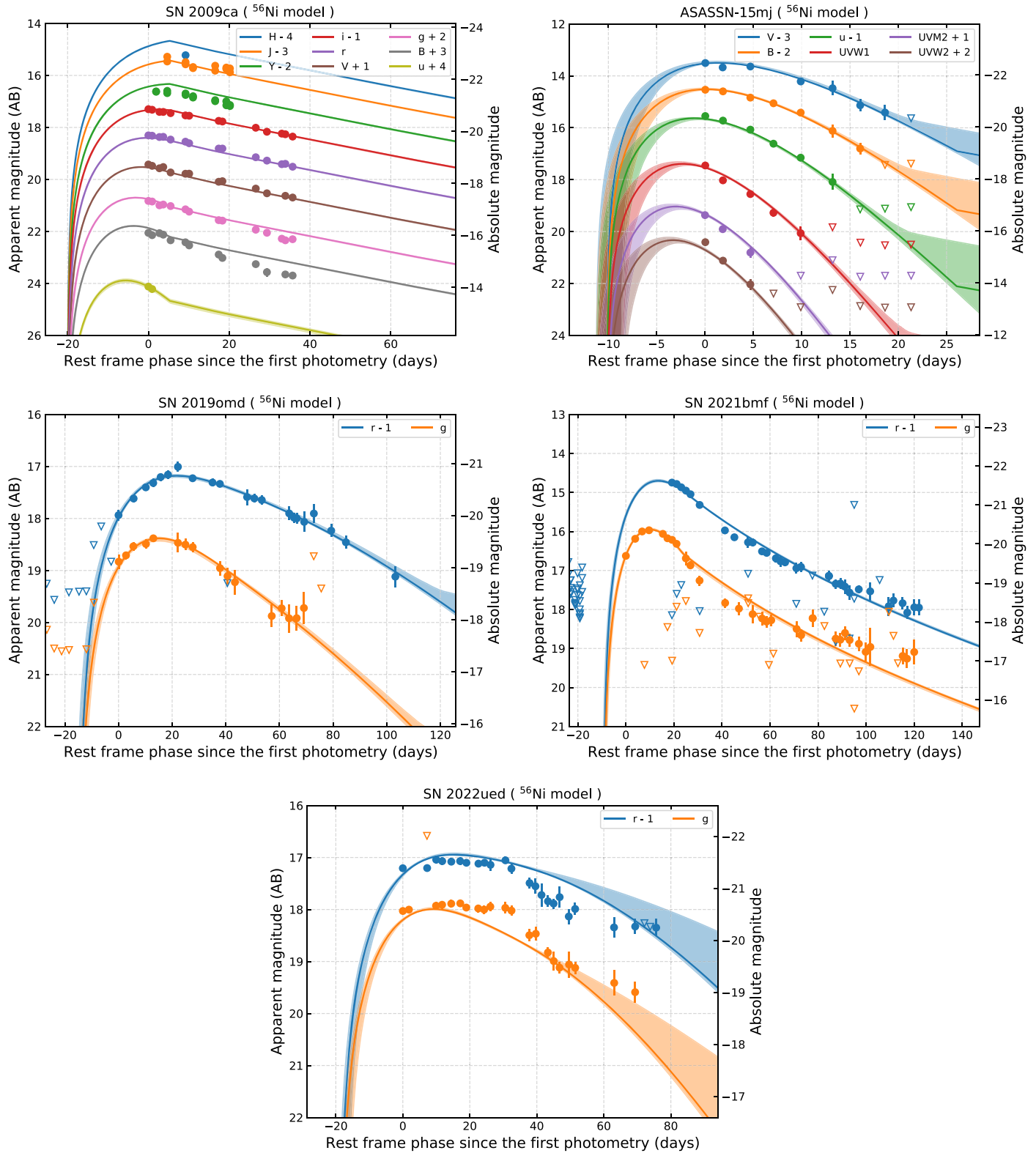


**Figure 1.** The best fits (the solid curves) of the multi-band LCs of SN 2009ca (the top-left panel), ASASSN-15mj (the top-right panel), SN 2019omd (the middle-left panel), SN 2021bmf (the middle-right panel), and SN 2022ued (the bottom panel) using the  $^{56}\text{Ni}$  model. The shaded regions indicate  $1\sigma$  bounds of the parameters. Circles represent observed data, triangles represent upper limits.

**Table 4**  
 Definitions, Units, and Prior Ranges of the Parameters of the Magnetar Plus  $^{56}\text{Ni}$ , and the Fallback Plus  $^{56}\text{Ni}$  Models<sup>a</sup>

Parameter	Definition	Unit	Prior
<b>Magnetar + <math>^{56}\text{Ni}</math> models</b>			
$M_{\text{ej}}$	The ejecta mass	$M_{\odot}$	[0.1, 50]
$P_0$	The initial period of the magnetar	ms	[0.8, 50]
$B$	The magnetic field strength of the magnetar	$10^{14}$ G	[0.1, 100]
$v_{\text{ph}}$	The early-time photospheric velocity	$10^9$ cm s <sup>-1</sup>	[0.1, 5]
$M_{\text{Ni}}$	The $^{56}\text{Ni}$ mass	$M_{\odot}$	[0, $0.2M_{\text{ej}}$ ]
$\log \kappa_{\gamma, \text{mag}}$	The $\gamma$ -ray opacity of magnetar photons	cm <sup>2</sup> g <sup>-1</sup>	[-2, 4]
$\log \kappa_{\gamma, \text{Ni}}$	The $\gamma$ -ray opacity of $^{56}\text{Ni}$ -cascade-decay photons	cm <sup>2</sup> g <sup>-1</sup>	[-1.568, 4]
$T_{\text{f}}$	The temperature floor of the photosphere	K	[1000, $10^4$ ]
$t_{\text{shift}}$	The explosion time relative to the first data	day	[-20, 0]
$A_{\text{host, V}}$	The extinction in the host galaxy	mag	[0, 1]
$\lambda_{\text{CF}}$	The cutoff wavelength	Å	[0, 4000]
$\beta'$	The dimensionless free parameter		[0, 10]
$\chi^2/\text{dof}$			
<b>Fallback + <math>^{56}\text{Ni}</math> models</b>			
$M_{\text{ej}}$	The ejecta mass	$M_{\odot}$	[0.1, 50]
$\log L_1$	The constant injection luminosity	erg s <sup>-1</sup>	[48, 58]
$\log t_{\text{tr, fb}}$	The transition time	day	[-3, 3]
$v_{\text{ph}}$	The early-time photospheric velocity	$10^9$ cm s <sup>-1</sup>	[0.1, 5]
$M_{\text{Ni}}$	The $^{56}\text{Ni}$ mass	$M_{\odot}$	[0, $0.2M_{\text{ej}}$ ]
$\log \kappa_{\gamma, \text{fb}}$	The $\gamma$ -ray opacity of fallback photons	cm <sup>2</sup> g <sup>-1</sup>	[-2, 4]
$\log \kappa_{\gamma, \text{Ni}}$	The $\gamma$ -ray opacity of $^{56}\text{Ni}$ -cascade-decay photons	cm <sup>2</sup> g <sup>-1</sup>	[-1.568, 4]
$T_{\text{f}}$	The temperature floor of the photosphere	K	[1000, $10^4$ ]
$t_{\text{shift}}$	The explosion time relative to the first data	day	[-20, 0]
$A_{\text{host, V}}$	The extinction in the host galaxy	mag	[0, 1]
$\lambda_{\text{CF}}$	The cutoff wavelength	Å	[0, 4000]
$\beta'$	The dimensionless free parameter		[0, 10]
$\chi^2/\text{dof}$			

**Note.**

<sup>a</sup> For SNe without UV photometric data,  $\lambda_{\text{CF}}$  and  $\beta'$  are set to be 3000 Å and 1, respectively.

Umeda & Nomoto (2008) suggest that the upper limit of the value of  $f$  of CCSNe is 0.2. Therefore, ASASSN-15mj, SN 2021bmf, and SN 2022ued cannot be explained by the  $^{56}\text{Ni}$  model. Although  $f$  of SN 2009ca and SN 2019omd is smaller than 0.2, the derived  $^{56}\text{Ni}$  mass of SN 2019omd is  $0.99 M_{\odot}$ , which is about twice those of some very energetic SNe Ic (e.g., SN 1998bw, SN 2003dh). Hence, we suggest that the  $^{56}\text{Ni}$  mass of SN 2019omd is also unreasonable. Finally, the possibility that SN 2009ca was powered by  $^{56}\text{Ni}$  decay cannot be excluded, since its  $^{56}\text{Ni}$  mass derived ( $0.56 M_{\odot}$ ) is comparable to those of SN 1998bw, SN 2003dh, and other energetic SNe Ic.

**2.2. Modeling the Multi-band LCs of Four LSNe Using the Magnetar Plus  $^{56}\text{Ni}$  Model and the Fallback Plus  $^{56}\text{Ni}$  Model**

Here, we use the magnetar plus  $^{56}\text{Ni}$  model and the fallback plus  $^{56}\text{Ni}$  model to fit the multi-band LCs of ASASSN-15mj, SN 2019omd, SN 2021bmf, and SN 2022ued. The details of the

two models can be found in Wang & Gan (2022) and Wang et al. (2023) and references therein; definitions, units, and prior ranges of the free parameters of the two models are listed in Table 4.

The fits of the two models for the four SNe are shown in Figure 2. The parameters and the corresponding corner plots are presented in Table 5 and Figures A6–A13. We find that the LCs of four SNe can be well fitted by the two models. The  $\chi^2/\text{dof}$  values of the best fits of ASASSN-15mj, SN 2019omd, SN 2021bmf, and SN 2022ued using the magnetar plus  $^{56}\text{Ni}$  model (the fallback plus  $^{56}\text{Ni}$  model) are respectively 0.82 (1.10), 0.55 (0.58), 0.93 (1.00), and 1.90 (2.01), indicating that the magnetar plus  $^{56}\text{Ni}$  model is better than the fallback plus  $^{56}\text{Ni}$  model for the four LSNe.

Based on the derived  $M_{\text{ej}}$  and  $v_{\text{ph}}$ , we can calculate the values of  $E_{\text{K}}$  of the SNe. For the magnetar plus  $^{56}\text{Ni}$  model (the fallback plus  $^{56}\text{Ni}$  model),  $E_{\text{K}}$  of ASASSN-15mj, SN 2019omd, SN 2021bmf, and SN 2022ued are  $2.84 \times 10^{50}$  erg ( $2.25 \times 10^{50}$  erg),  $2.38 \times 10^{51}$  erg ( $2.53 \times 10^{50}$  erg),  $3.35 \times 10^{52}$  erg

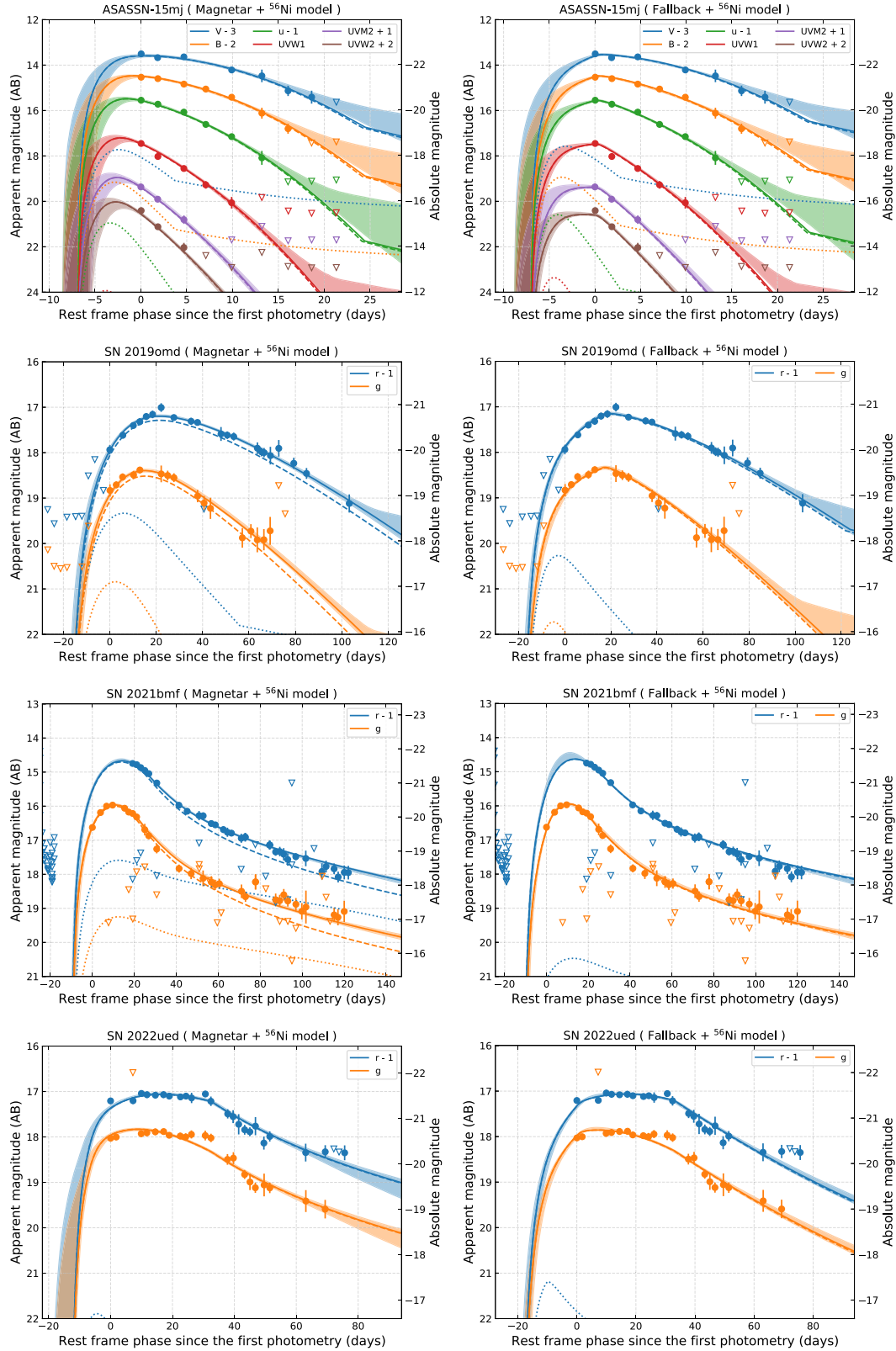


**Figure 2.** The best fits (the solid curves) of the multi-band LCs of ASASSN-15mj, SN 2019omd, SN 2021bmf, and SN 2022ued using the magnetar plus  $^{56}\text{Ni}$  model (the left panels) and the fallback plus  $^{56}\text{Ni}$  model (the right panels). The dotted lines are the LCs powered by the  $^{56}\text{Ni}$ , and the dashed lines are the LCs powered by the magnetar (the left panels) or the fallback (the right panels), respectively. The shaded regions indicate  $1\sigma$  bounds of the parameters. Circles represent observed data, triangles represent upper limits.

**Table 5**  
Medians,  $1\sigma$  Bounds, and Best-fitting Values (in Parentheses) of the Parameters of the Magnetar Plus  $^{56}\text{Ni}$  Model and the Fallback Plus  $^{56}\text{Ni}$  Model

Parameter	ASASSN-15mj	SN 2019omd	SN 2021bmf	SN 2022ued
<b>Magnetar + <math>^{56}\text{Ni}</math> Model</b>				
$M_{\text{ej}}(M_{\odot})$	$0.20^{+0.17}_{-0.09}$ (0.16)	$4.34^{+1.14}_{-1.17}$ (4.56)	$11.67^{+2.73}_{-2.04}$ (10.25)	$0.40^{+0.77}_{-0.18}$ (0.28)
$P_0(\text{ms})$	$10.65^{+3.12}_{-4.05}$ (8.96)	$6.76^{+0.76}_{-1.38}$ (7.40)	$4.41^{+0.68}_{-0.54}$ (3.96)	$2.78^{+0.85}_{-0.97}$ (2.31)
$B(10^{14} \text{ G})$	$15.49^{+2.13}_{-1.87}$ (15.84)	$2.05^{+0.30}_{-0.33}$ (1.76)	$4.24^{+0.72}_{-0.45}$ (4.15)	$2.87^{+0.18}_{-0.53}$ (2.97)
$v_{\text{ph}}(10^9 \text{ cm s}^{-1})$	$1.78^{+0.26}_{-0.25}$ (1.70)	$0.87^{+0.10}_{-0.09}$ (0.93)	$2.53^{+0.31}_{-0.23}$ (2.34)	$0.77^{+0.05}_{-0.08}$ (0.79)
$M_{\text{Ni}}(M_{\odot})$	$0.02^{+0.02}_{-0.01}$ (0.01)	$0.29^{+0.15}_{-0.19}$ (0.23)	$0.38^{+0.08}_{-0.13}$ (0.46)	$0.04^{+0.08}_{-0.03}$ (0.02)
$\log \kappa_{\gamma, \text{mag}}(\text{cm}^2 \text{ g}^{-1})$	$0.46^{+2.33}_{-1.30}$ (-0.53)	$1.43^{+1.74}_{-1.79}$ (3.09)	$1.56^{+1.66}_{-1.68}$ (0.12)	$1.32^{+1.83}_{-2.29}$ (2.46)
$\log \kappa_{\gamma, \text{Ni}}(\text{cm}^2 \text{ g}^{-1})$	$1.20^{+1.94}_{-1.93}$ (3.11)	$1.24^{+1.89}_{-1.88}$ (0.58)	$1.40^{+1.77}_{-1.75}$ (-0.33)	$1.25^{+1.86}_{-1.91}$ (1.46)
$T_{\text{f}}(\text{K})$	$3494.34^{+1614.20}_{-1682.38}$ (3890.14)	$2614.09^{+1092.47}_{-1095.00}$ (2933.49)	$6884.81^{+428.77}_{-468.09}$ (7011.24)	$9888.57^{+83.03}_{-176.52}$ (9962.00)
$t_{\text{shift}}(\text{day})$	$-6.86^{+1.28}_{-1.72}$ (-6.88)	$-16.92^{+2.04}_{-1.82}$ (-16.73)	$-9.33^{+0.86}_{-0.82}$ (-9.62)	$-13.81^{+1.95}_{-5.59}$ (-12.47)
$A_{\text{host, v}}(\text{mag})$	$0.29^{+0.14}_{-0.13}$ (0.34)	$0.35^{+0.36}_{-0.26}$ (0.11)	$0.76^{+0.17}_{-0.22}$ (0.86)	$0.12^{+0.08}_{-0.07}$ (0.15)
$\lambda_{\text{CF}}(\text{\AA})$	$3543.41^{+89.87}_{-103.25}$ (3598.72)	...	...	...
$\beta$	$2.50^{+0.43}_{-0.39}$ (2.62)	...	...	...
$\chi^2/\text{dof}$	1.59 (0.82)	0.79 (0.55)	0.99 (0.93)	2.00 (1.90)
<b>Fallback + <math>^{56}\text{Ni}</math> model</b>				
$M_{\text{ej}}(M_{\odot})$	$0.13^{+0.04}_{-0.02}$ (0.11)	$1.35^{+0.98}_{-0.63}$ (0.77)	$14.36^{+6.84}_{-2.90}$ (12.16)	$0.43^{+0.30}_{-0.22}$ (0.23)
$\log L_1(\text{erg s}^{-1})$	$53.46^{+0.06}_{-0.06}$ (53.45)	$54.80^{+0.05}_{-0.05}$ (54.81)	$54.47^{+0.09}_{-0.09}$ (54.46)	$54.89^{+0.05}_{-0.05}$ (54.92)
$\log t_{\text{tr, fb}}(\text{day})$	$0.89^{+0.06}_{-0.06}$ (0.85)	$1.53^{+0.03}_{-0.05}$ (1.54)	$1.01^{+0.03}_{-0.03}$ (1.01)	$1.30^{+0.04}_{-0.05}$ (1.27)
$v_{\text{ph}}(10^9 \text{ cm s}^{-1})$	$1.82^{+0.17}_{-0.16}$ (1.85)	$0.73^{+0.04}_{-0.04}$ (0.74)	$2.88^{+1.51}_{-0.35}$ (2.56)	$0.69^{+0.04}_{-0.03}$ (0.70)
$M_{\text{Ni}}(M_{\odot})$	$0.01^{+0.01}_{-0.01}$ (0.01)	$0.14^{+0.17}_{-0.10}$ (0.12)	$0.08^{+0.11}_{-0.06}$ (0.03)	$0.04^{+0.05}_{-0.03}$ (0.04)
$\log \kappa_{\gamma, \text{fb}}(\text{cm}^2 \text{ g}^{-1})$	$0.70^{+2.24}_{-1.11}$ (-0.28)	$1.61^{+1.63}_{-1.64}$ (3.08)	$1.29^{+1.84}_{-1.59}$ (1.91)	$-0.86^{+0.32}_{-0.25}$ (-0.60)
$\log \kappa_{\gamma, \text{Ni}}(\text{cm}^2 \text{ g}^{-1})$	$1.17^{+1.92}_{-1.89}$ (1.04)	$1.29^{+1.83}_{-1.86}$ (1.69)	$0.70^{+2.24}_{-1.83}$ (-0.49)	$1.29^{+1.84}_{-1.84}$ (2.83)
$T_{\text{f}}(\text{K})$	$3266.25^{+1541.29}_{-1534.51}$ (3919.21)	$3022.61^{+1454.40}_{-1383.00}$ (3650.16)	$6868.95^{+696.32}_{-536.67}$ (6545.46)	$9881.31^{+87.81}_{-174.13}$ (9966.10)
$t_{\text{shift}}(\text{day})$	$-7.68^{+1.02}_{-1.22}$ (-7.04)	$-18.68^{+1.51}_{-0.94}$ (-17.87)	$-9.90^{+0.66}_{-0.60}$ (-10.25)	$-18.82^{+1.66}_{-0.87}$ (-18.02)
$A_{\text{host, v}}(\text{mag})$	$0.26^{+0.11}_{-0.11}$ (0.27)	$0.81^{+0.11}_{-0.11}$ (0.81)	$0.69^{+0.20}_{-0.20}$ (0.65)	$0.10^{+0.06}_{-0.06}$ (0.14)
$\lambda_{\text{CF}}(\text{\AA})$	$3481.23^{+75.91}_{-77.34}$ (3539.12)	...	...	...
$\beta$	$2.22^{+0.31}_{-0.30}$ (2.44)	...	...	...
$\chi^2/\text{dof}$	1.44 (1.10)	0.64 (0.58)	1.18 (1.00)	2.09 (2.01)

**Note.** The values of  $\chi^2/\text{dof}$  (reduced  $\chi^2$ , dof = degree of freedom) are also presented.

( $4.76 \times 10^{52}$  erg), and  $1.07 \times 10^{50}$  erg ( $6.78 \times 10^{49}$  erg), respectively. Using Equation (1), the  $^{56}\text{Ni}$  masses of ASASSN-15mj, SN 2019omd, SN 2021bmf, and SN 2022ued derived by the magnetar plus  $^{56}\text{Ni}$  model (the fallback plus  $^{56}\text{Ni}$  model) are  $0.01 M_{\odot}$  ( $0.01 M_{\odot}$ ),  $0.11 M_{\odot}$  ( $0.07 M_{\odot}$ ),  $0.21 M_{\odot}$  ( $0.01 M_{\odot}$ ), and  $0.02 M_{\odot}$  ( $0.03 M_{\odot}$ ), respectively.

For the magnetar plus  $^{56}\text{Ni}$  model, the derived values of  $M_{\text{ej}}$ ,  $M_{\text{Ni}}$ ,  $P_0$ ,  $B$ ,  $v_{\text{ph}}$ , and  $E_{\text{K}}$  are  $\sim(0.1\text{--}10) M_{\odot}$ ,  $\sim(0.01\text{--}0.5) M_{\odot}$ ,  $\sim(2\text{--}9)$  ms,  $\sim(1\text{--}15) \times 10^{14}$  G,  $\sim(0.7\text{--}2.4) \times 10^9$  cm s $^{-1}$ , and  $\sim(0.10\text{--}35.0) \times 10^{51}$  erg, respectively; the mean values of these parameters are  $\sim 3.81 M_{\odot}$ ,  $\sim 0.18 M_{\odot}$ ,  $\sim 5.66$  ms,  $\sim 6.18 \times 10^{14}$  G,  $\sim 1.44 \times 10^9$  cm s $^{-1}$ , and  $9.07 \times 10^{51}$  erg, respectively.

For the fallback plus  $^{56}\text{Ni}$  model, the derived values of  $M_{\text{ej}}$ ,  $M_{\text{Ni}}$ ,  $L_1$ ,  $t_{\text{tr, fb}}$ ,  $v_{\text{ph}}$ , and  $E_{\text{K}}$  are  $\sim(0.1\text{--}12) M_{\odot}$ ,  $\sim(0.01\text{--}0.1) M_{\odot}$ ,  $\sim(0.2\text{--}8) \times 10^{54}$  erg s $^{-1}$ ,  $\sim(7\text{--}35)$  days,  $\sim(0.7\text{--}2.6) \times 10^9$  cm s $^{-1}$ , and  $\sim(0.10\text{--}48.0) \times 10^{51}$  erg, respectively; the mean values of these parameters are  $\sim 3.32 M_{\odot}$ ,  $\sim 0.05 M_{\odot}$ ,

$\sim 4.49 \times 10^{54}$  erg s $^{-1}$ ,  $\sim 17.65$  days,  $\sim 1.46 \times 10^9$  cm s $^{-1}$ , and  $\sim 1.20 \times 10^{52}$  erg, respectively.

The derived  $M_{\text{Ni}}$  of the magnetar plus  $^{56}\text{Ni}$  model and the fallback plus  $^{56}\text{Ni}$  model are respectively  $\sim 0.01\text{--}0.21 M_{\odot}$  and  $\sim 0.01\text{--}0.07 M_{\odot}$ , which are consistent with those of normal SNe Ic. Moreover, other parameters of the two models are also in reasonable ranges and comparable to those derived in the literature (e.g., Wang et al. 2015b; Gomez et al. 2022). Therefore, we suggest both the magnetar plus  $^{56}\text{Ni}$  model and the fallback plus  $^{56}\text{Ni}$  model are reasonable.

### 3. Discussion

#### 3.1. The Masses of the Ejecta of ASASSN-15mj and SN 2022ued

The ejecta masses for ASASSN-15mj and SN 2022ued are  $0.16 M_{\odot}$  and  $0.28 M_{\odot}$  (the magnetar plus  $^{56}\text{Ni}$  model), and  $0.11 M_{\odot}$  and  $0.23 M_{\odot}$  (the fallback plus  $^{56}\text{Ni}$  model),

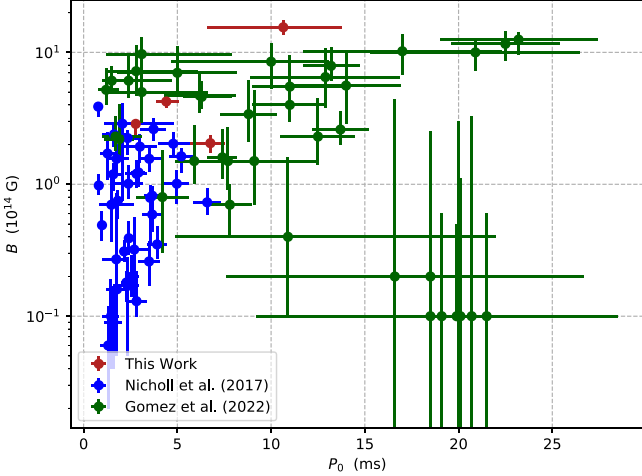


**Figure 3.** The  $P_0$ - $B$  distribution of the magnetar of the four LSNe (ASASSN-15mj, SN 2019omd, SN 2021bmf, and SN 2022ued) in our sample (red dots). For comparison, the  $P_0$ - $B$  distributions of the magnetar of SLSNe in Nicholl et al. (2017) and LSNe in Gomez et al. (2022) are also plotted (blue and green dots, respectively).

respectively. These values are significantly lower than the range of ejecta masses of SLSNe and normal Ib/c SNe in the literature which are 1–40  $M_\odot$  (Blanchard et al. 2020) and 1–10  $M_\odot$  (Prentice et al. 2019), respectively.

The small derived ejecta masses of the two SNe might be due to the absence of pre-peak data which results in poor constraints for the rise time and therefore the ejecta masses. Otherwise, the two SNe are ultra-stripped LSN like iPTF16asu (Whitesides et al. 2017; Wang & Gan 2022).

### 3.2. Comparison with Previous Studies

Assuming that ASASSN-15mj, SN 2019omd, SN 2021bmf, and SN 2022ued are powered mainly by magnetars, we plot the distribution of  $P_0$  and  $B$  (see Table 5) of the magnetars assumed to power the LCs of the four LSNe that we study and those of the magnetars associated with the LSNe studied by Gomez et al. (2022) and the SLSNe studied by Nicholl et al. (2017), see Figure 3. It can be found that the parameter space of the putative magnetars powering the LCs of the four SNe that we study overlaps both that of the LSNe studied by Gomez et al. (2022) and the SLSNe studied by Nicholl et al. (2017). Moreover, the derived upper limit of  $P_0$  ( $\sim 11$  ms) of our sample is smaller than that ( $\sim 23$  ms) of Gomez et al. (2022), while the derived lower limit of  $P_0$  ( $\sim 3$  ms) of our sample is larger than that ( $\sim 1$  ms) of Nicholl et al. (2017). This is because the peak absolute magnitudes of our sample are in  $-19.5$  to  $-20.5$  mag, while the peak absolute magnitudes of Gomez et al. (2022) and Nicholl et al. (2017) extend to  $-19$  and  $< -21$  mag, respectively.

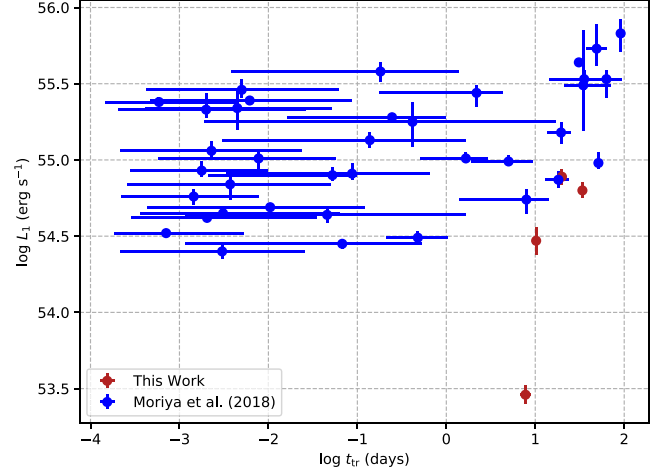


**Figure 4.** The  $\log L_1$ - $\log t_{\text{tr}}$  distributions of the fallback plus  $^{56}\text{Ni}$  model for the four LSNe (ASASSN-15mj, SN 2019omd, SN 2021bmf, and SN 2022ued) in our sample (red dots). For comparison, the  $\log L_1$ - $\log t_{\text{tr}}$  distributions of the fallback model for SLSNe in Moriya et al. (2018a) are also plotted (blue dots).

Assuming that ASASSN-15mj, SN 2019omd, SN 2021bmf, and SN 2022ued are powered mainly by fallback, we plot the distribution of  $L_1$  and  $t_{\text{tr}}$  (see Table 5) of the four LSNe and those of SLSNe studied by Moriya et al. (2018a), see Figure 4. It can be found that the parameters of the four SNe we study are located in the lower right of the parameter space (larger  $t_{\text{tr}}$  and lower  $L_1$ ) while the parameters of SLSNe studied by Moriya et al. (2018a) are located mainly in the upper left of the parameter space (smaller  $t_{\text{tr}}$  and higher  $L_1$ ). It should be noted that, however, there is a small overlap between our sample and the sample of Moriya et al. (2018a).

### 3.3. The Accretion Masses and the Validity of the Fallback Plus $^{56}\text{Ni}$ Model

For the fallback plus  $^{56}\text{Ni}$  model, the accretion mass  $M_{\text{acc}}$  can be written as (Moriya et al. 2018a)

$$\eta M_{\text{acc}} c^2 = 2.5 L_1 t_{\text{tr,fb}}^{-2/3} \quad (2)$$

here,  $\eta$  is the efficiency of converting accretion to input energy which can be from  $\sim 0.001$  (Dexter & Kasen 2013) to  $\sim 0.1$  (e.g., McKinney 2005; Kumar et al. 2008; Gilkis et al. 2016). Using the equation, the accretion masses of the four LSNe are 0.0005–0.0547  $M_\odot$ , 0.0043–0.4345  $M_\odot$ , 0.0043–0.4378  $M_\odot$ , 0.0084–0.8472  $M_\odot$ , respectively. The accretion masses are significantly smaller than the derived  $^{56}\text{Ni}$  masses if  $\eta$  is set to be the upper limit (0.1). In contrast, the accretion masses are larger than the derived  $^{56}\text{Ni}$  masses if  $\eta$  is set to be the lower limit (0.001). Therefore, the validity of the fallback plus  $^{56}\text{Ni}$  model depends on the value of  $\eta$  and favors a large  $\eta$  value.

#### 4. Conclusions

In this paper, we study five LSNe with  $M_{\text{peak}} \approx -19.5$  to  $-21$  mag by fitting their multi-band LCs with different energy source models. We find that the  $^{56}\text{Ni}$  model cannot account for the LCs of four SNe (ASASSN-15mj, SN 2019omd, SN 2002ued, and SN 2021bmf) in our sample, since  $f$  of the three SNe (ASASSN-15mj, SN 2002ued, and SN 2021bmf) are larger than the upper limit (0.2) of  $f$  value of CCSNe, while the derived  $^{56}\text{Ni}$  mass of SN 2019omd is  $0.99 M_{\odot}$ , which is about twice those of some very energetic SNe Ic. For comparison, the derived  $^{56}\text{Ni}$  mass ( $0.56 M_{\odot}$ ) of SN 2009ca is comparable to those of energetic SNe Ic, indicating that it might be powered by the  $^{56}\text{Ni}$  cascade decay. This indicates that some LSNe might be powered by  $^{56}\text{Ni}$  cascade decay, though most of them need additional energy sources.

We use the magnetar plus  $^{56}\text{Ni}$  model and the fallback plus  $^{56}\text{Ni}$  model to fit the LCs of the four LSNe that cannot be explained by the  $^{56}\text{Ni}$  model, finding that the two models can account for the four SNe. The  $\chi^2/\text{dof}$  values of the best fits of the two models suggest that the magnetar plus  $^{56}\text{Ni}$  model is better than the fallback plus  $^{56}\text{Ni}$  model for the four LSNe.

For the magnetar plus  $^{56}\text{Ni}$  model,  $M_{\text{ej}}$ ,  $M_{\text{Ni}}$ ,  $P_0$ ,  $B$ ,  $v_{\text{ph}}$ , and  $E_{\text{K}}$  are  $\sim(0.2-10) M_{\odot}$ ,  $<0.3 M_{\odot}$ ,  $\sim(2-9)$  ms,  $\sim(1-15) \times 10^{14}$  G,  $\sim(0.7-2.4) \times 10^9$  cm s $^{-1}$ , and  $\sim(0.10-35.0) \times 10^{51}$  erg, respectively. These values are comparable to the typical values of the magnetars supposed to power the LCs of LSNe (see, e.g., Wang et al. 2015b; Gomez et al. 2022) and some SLSNe (see, e.g., Nicholl et al. 2017). For the fallback plus  $^{56}\text{Ni}$  model,  $M_{\text{ej}}$ ,  $M_{\text{Ni}}$ ,  $L_1$ ,  $t_{\text{tr,fb}}$ ,  $v_{\text{ph}}$ , and  $E_{\text{K}}$  are  $\sim(0.1-12) M_{\odot}$ ,  $\sim(0.01-0.1) M_{\odot}$ ,  $\sim(0.2-8) \times 10^{54}$  erg s $^{-1}$ ,  $\sim(7-35)$  day,  $\sim(0.7-2.6) \times 10^9$  cm s $^{-1}$ , and  $\sim(0.10-48.0) \times 10^{51}$  erg, respectively.

It should be noted that, however, the derived  $M_{\text{ej}}$  of ASASSN-15mj and SN 2022ued are respectively  $0.16 M_{\odot}$  ( $0.11 M_{\odot}$ ) and  $0.28 M_{\odot}$  ( $0.23 M_{\odot}$ ) for the magnetar plus  $^{56}\text{Ni}$  model (the fallback plus  $^{56}\text{Ni}$  model), which are comparable to those of ultra-stripped SNe. This might be due to the absence of pre-peak data which prevents us from better constraining the

rise time and therefore the ejecta masses; or the two SNe are ultra-stripped LSN like iPTF16asu.

Finally, we find that the distribution of  $P_0$  and  $B$  of the putative magnetars powering the LCs of the four SNe overlaps those of the magnetars of LSNe and SLSNe in the literature, if they are (mainly) powered by magnetars. Similarly, the distribution of  $L_1$  and  $t_{\text{tr}}$  of the fallback powering the LCs of the four SNe overlaps those of the fallback of SLSNe in the literature, if they are (mainly) powered by fallback.

We suggest that the magnetar plus  $^{56}\text{Ni}$  model is more reasonable than the fallback plus  $^{56}\text{Ni}$  model, since the validity of the fallback plus  $^{56}\text{Ni}$  model depends on the value of  $\eta$  and favors a large  $\eta$  value, and the magnetar plus  $^{56}\text{Ni}$  model yields smaller  $\chi^2/\text{dof}$  values. It should be pointed out that, however, the fallback plus  $^{56}\text{Ni}$  model is still a promising model that can account for the four SNe in our sample as well as other LSNe.

#### Acknowledgments

We thank the anonymous referee for the helpful comments and suggestions that have allowed us to improve this manuscript. Song-Yao Bai thanks Deng-Wang Shi (石登旺), and Qiu-Ping Huang (黄秋萍) for their helpful discussion. This work is supported by the National Natural Science Foundation of China (grant Nos. 11963001, 12133003, 11833003, 11973020 (C0035736), and U1938201).

#### Appendix

Figures A1–A5 are the corner plots of the  $^{56}\text{Ni}$  model of SN 2009ca, ASASSN-15mj, SN 2019omd, SN 2021bmf, and SN 2022ued, respectively. Figures A6–A9 are the corner plots of the magnetar plus  $^{56}\text{Ni}$  model of ASASSN-15mj, SN 2019omd, SN 2021bmf, and SN 2022ued, respectively. Figures A10–A13 are the corner plots of the fallback plus  $^{56}\text{Ni}$  model of ASASSN-15mj, SN 2019omd, SN 2021bmf, and SN 2022ued, respectively.

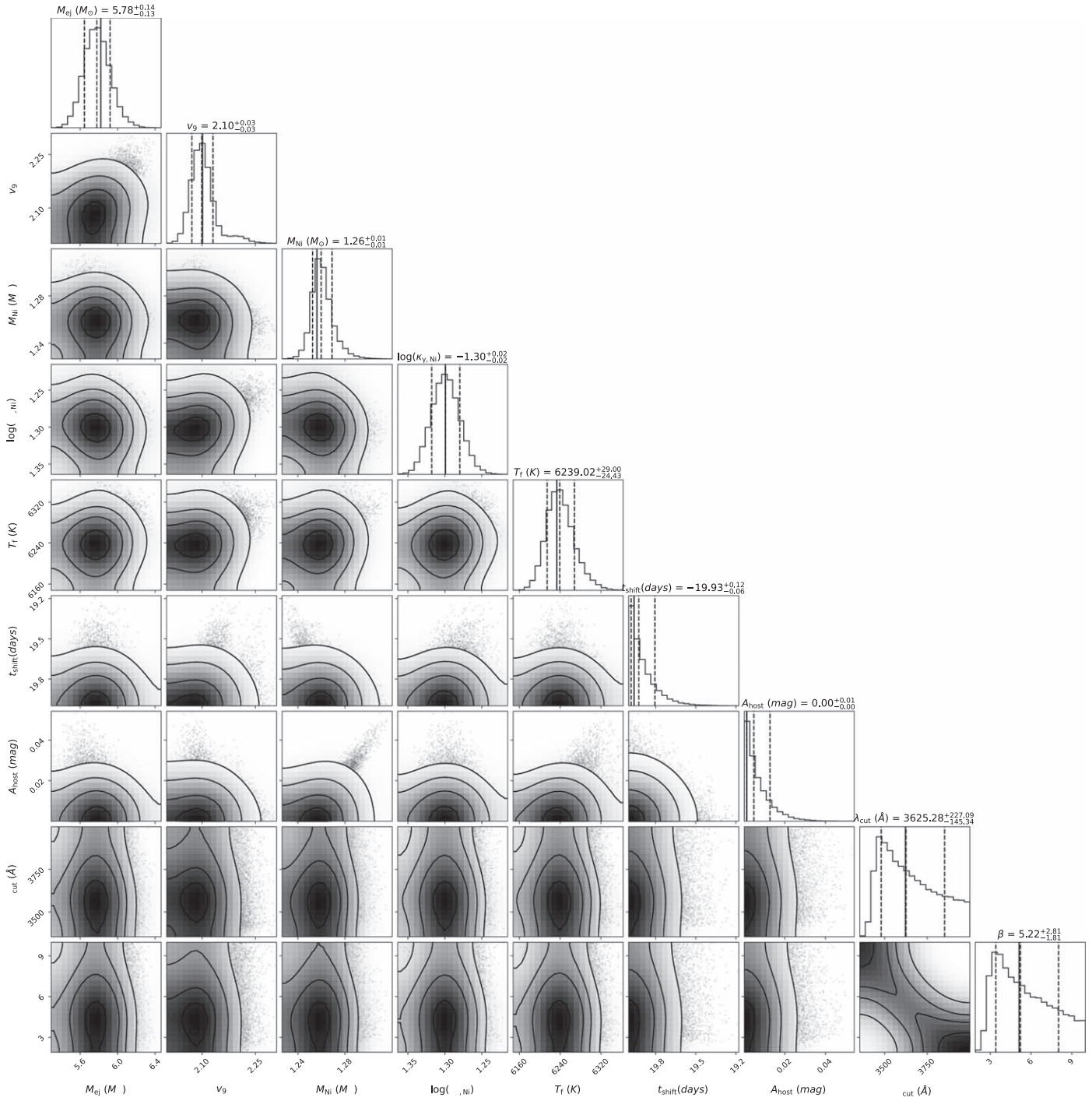


**Figure A1.** The corner plot of the  $^{56}\text{Ni}$  model for the multi-band LCs of SN 2009ca. The solid vertical lines represent the best-fitting parameters, while the dashed vertical lines represent the medians and the  $1\sigma$  bounds of the parameters.

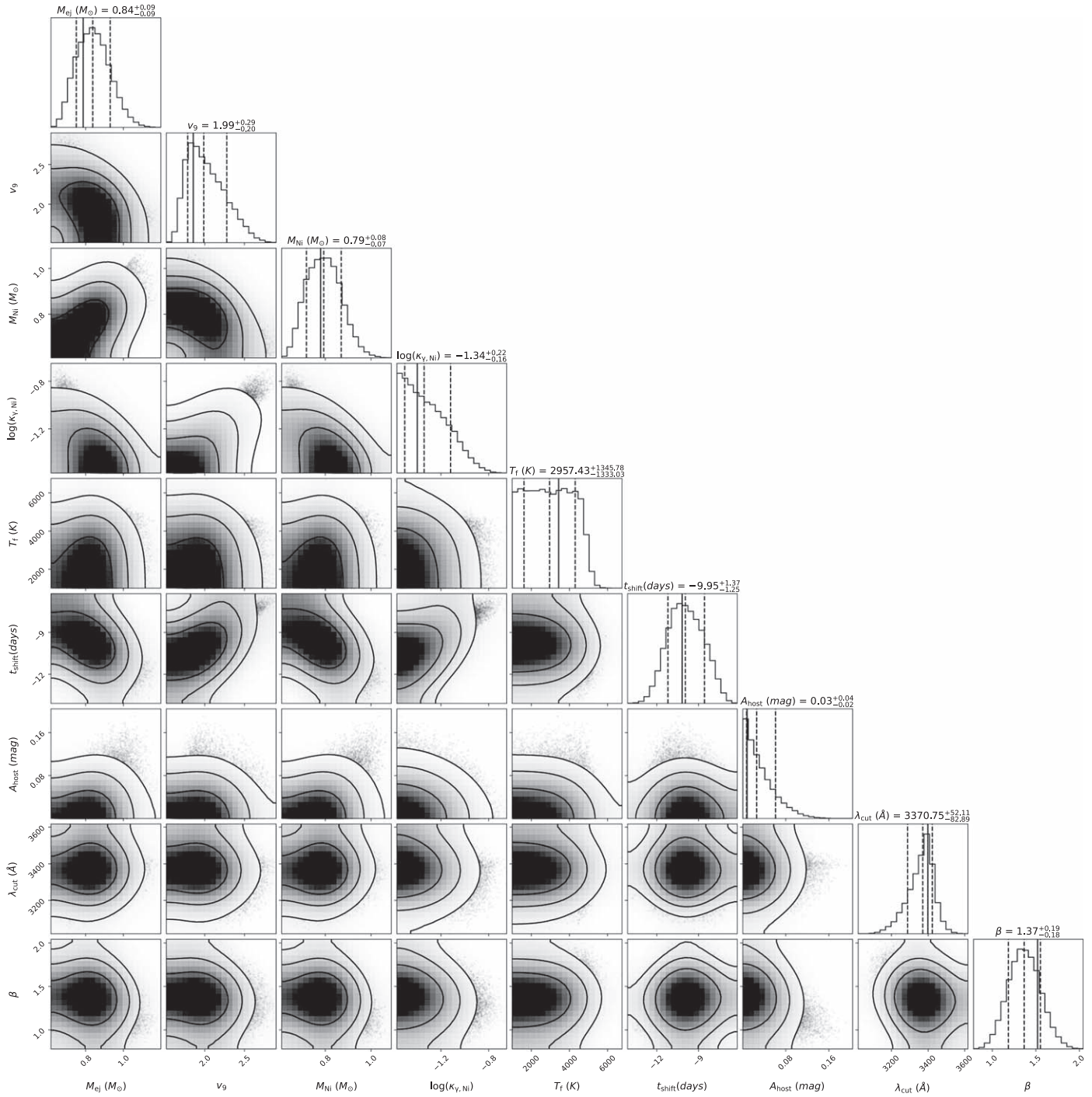


**Figure A2.** The corner plot of the  $^{56}\text{Ni}$  model for the multi-band LCs of ASASSN-15mj. The solid vertical lines represent the best-fitting parameters, while the dashed vertical lines represent the medians and the  $1\sigma$  bounds of the parameters.

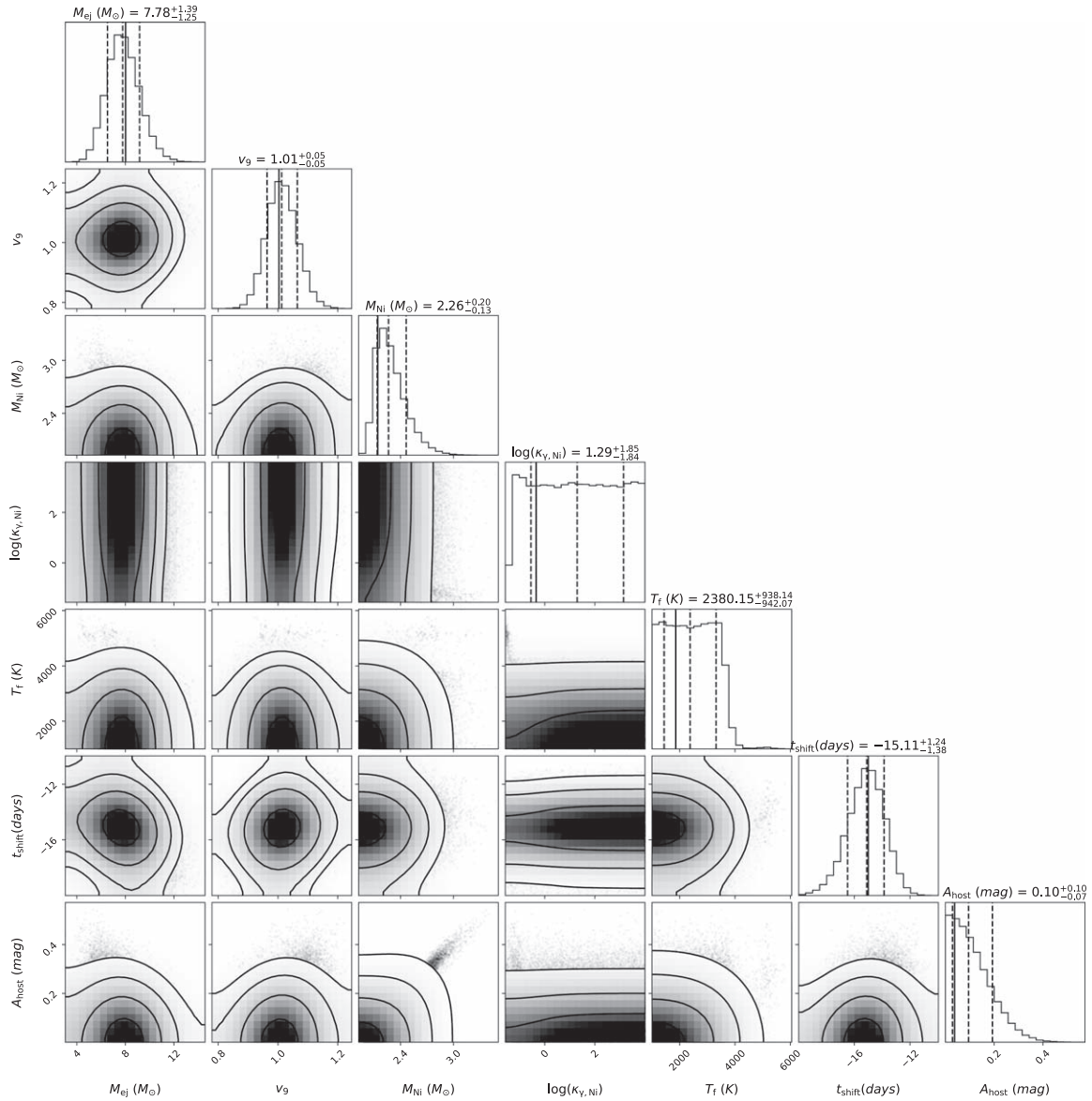


**Figure A3.** The corner plot of the  $^{56}\text{Ni}$  model for the multi-band LCs of SN 2019omd. The solid vertical lines represent the best-fitting parameters, while the dashed vertical lines represent the medians and the  $1\sigma$  bounds of the parameters.

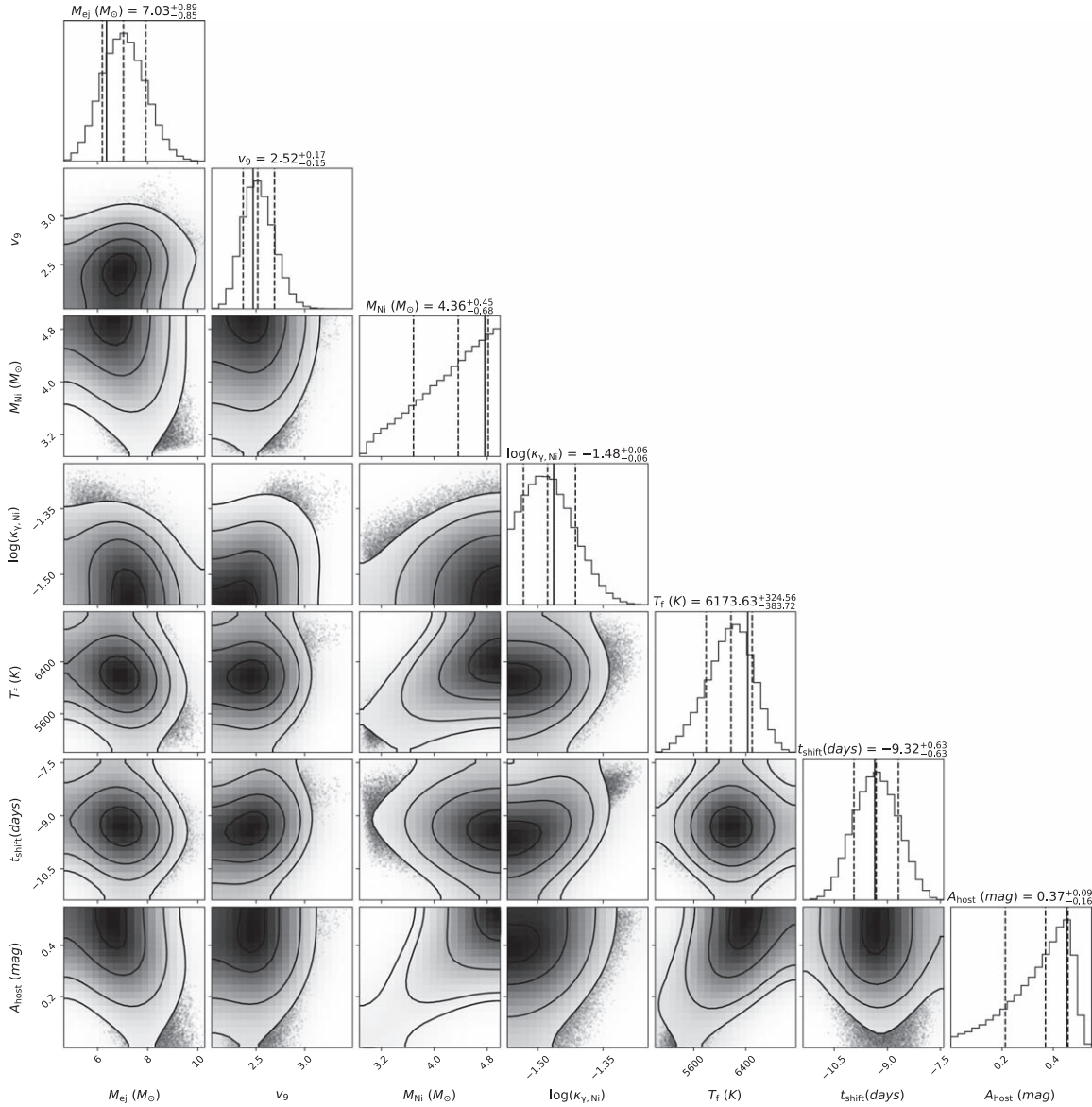


**Figure A4.** The corner plot of the  $^{56}\text{Ni}$  model for the multi-band LCs of SN 2021bmf. The solid vertical lines represent the best-fitting parameters, while the dashed vertical lines represent the medians and the  $1\sigma$  bounds of the parameters.

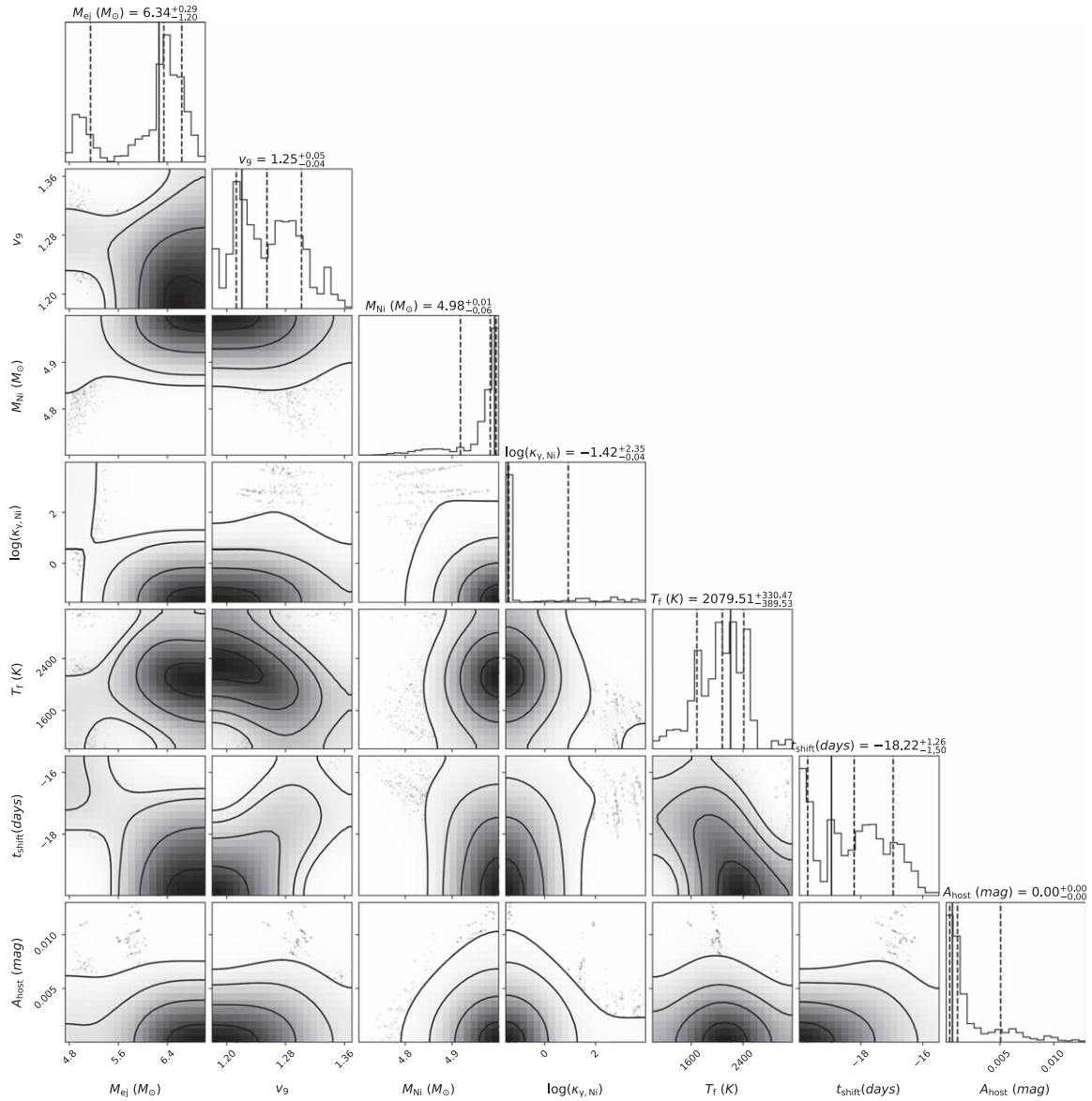


**Figure A5.** The corner plot of the  $^{56}\text{Ni}$  model for the multi-band LCs of SN 2022ued. The solid vertical lines represent the best-fitting parameters, while the dashed vertical lines represent the medians and the  $1\sigma$  bounds of the parameters.

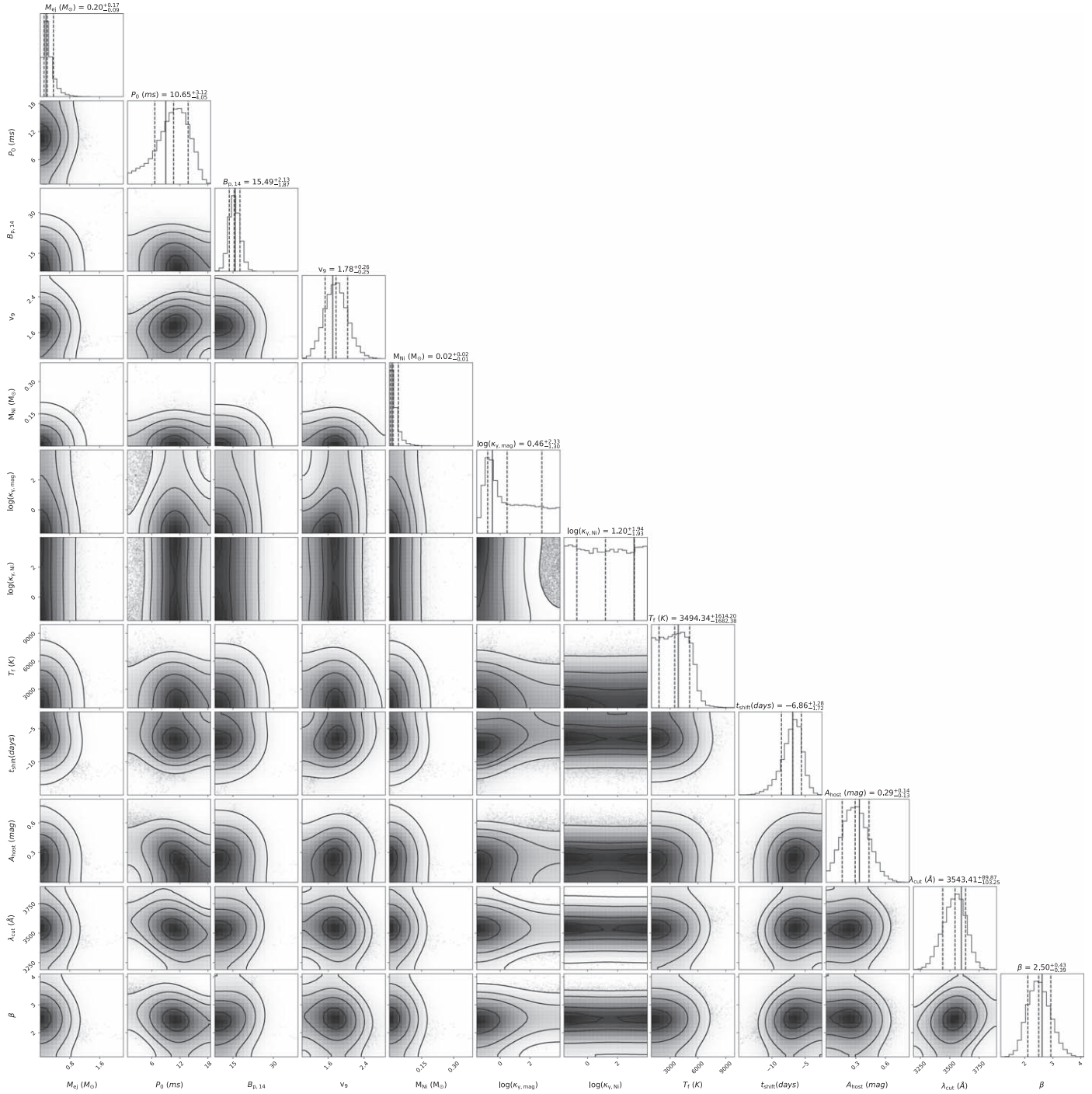


**Figure A6.** The corner plot of the magnetar plus  $^{56}\text{Ni}$  model for the multi-band LCs of ASASSN-15mj. The solid vertical lines represent the best-fitting parameters, while the dashed vertical lines represent the medians and the  $1\sigma$  bounds of the parameters.

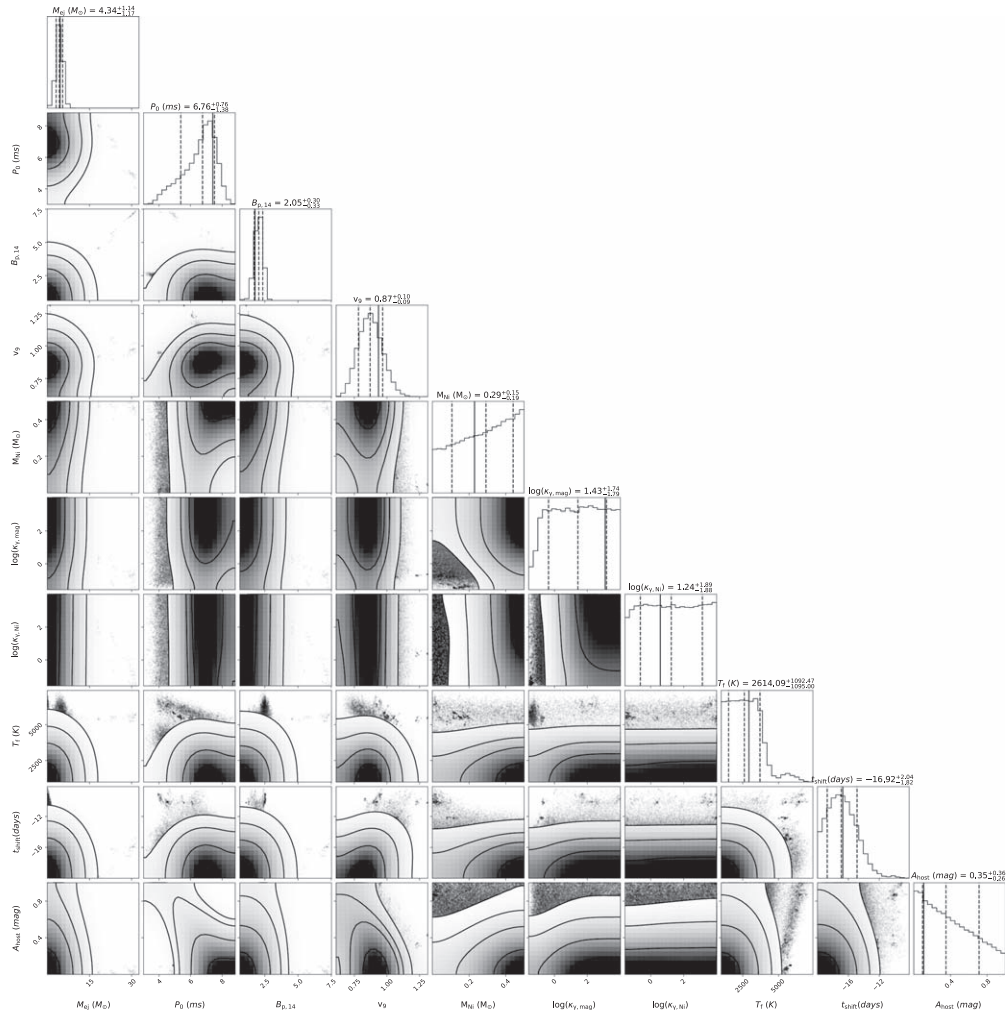


**Figure A7.** The corner plot of the magnetar plus  $^{56}\text{Ni}$  model for the multi-band LCs of SN 2019omd. The solid vertical lines represent the best-fitting parameters, while the dashed vertical lines represent the medians and the  $1\sigma$  bounds of the parameters.

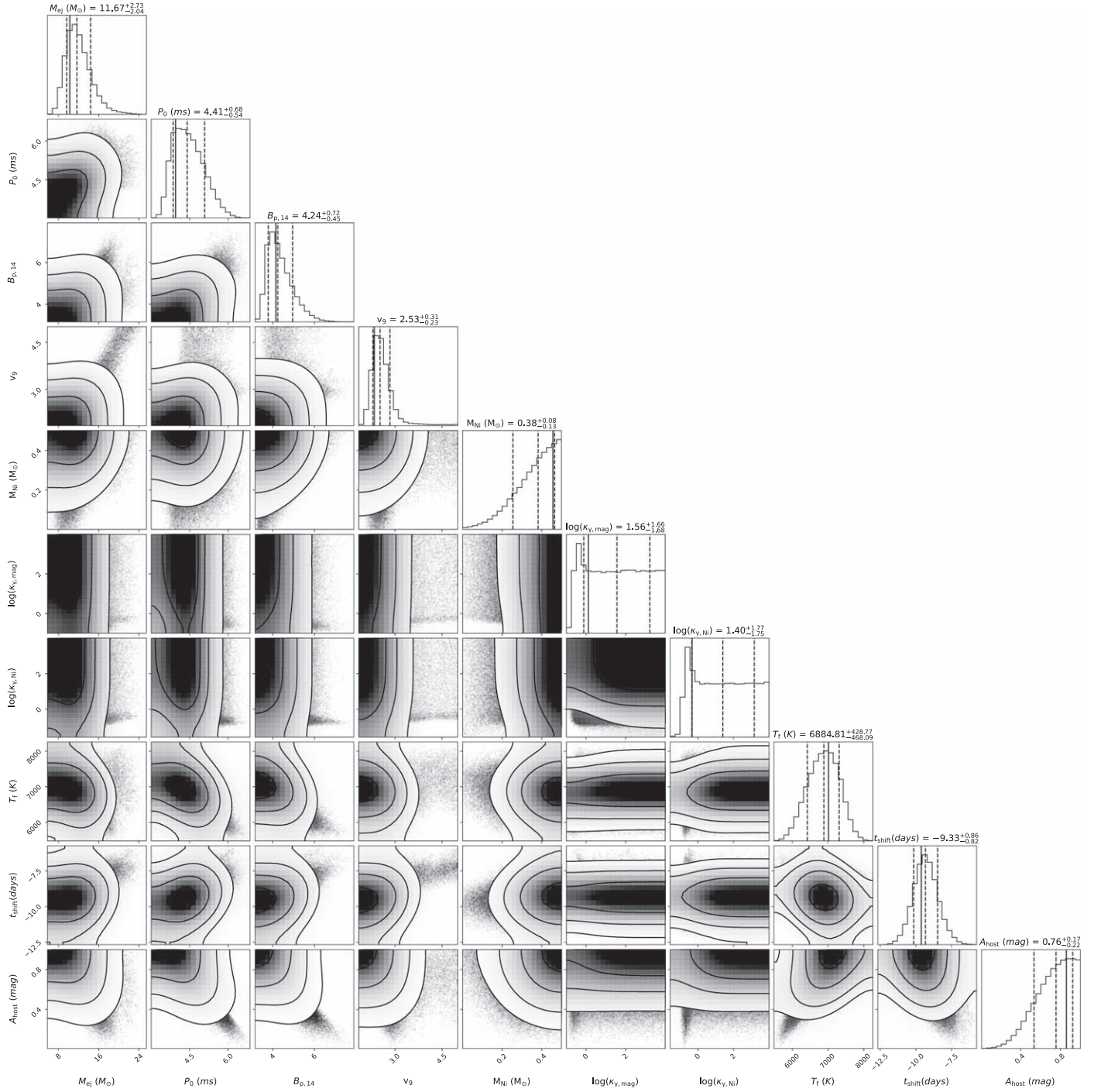


**Figure A8.** The corner plot of the magnetar plus  $^{56}\text{Ni}$  model for the multi-band LCs of SN 2021bmf. The solid vertical lines represent the best-fitting parameters, while the dashed vertical lines represent the medians and the  $1\sigma$  bounds of the parameters.

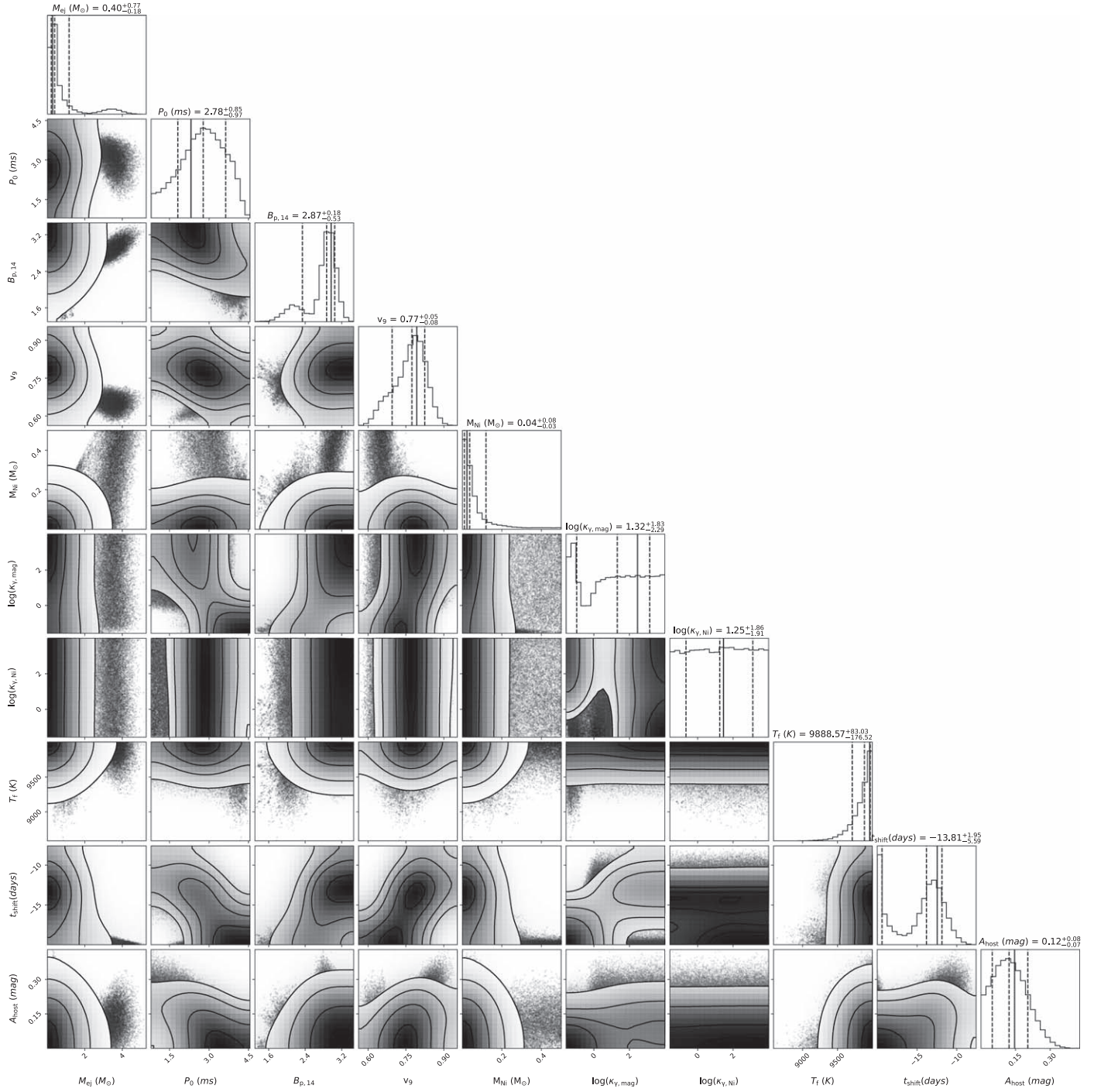


**Figure A9.** The corner plot of the magnetar plus  $^{56}\text{Ni}$  model for the multi-band LCs of SN 2022ued. The solid vertical lines represent the best-fitting parameters, while the dashed vertical lines represent the medians and the  $1\sigma$  bounds of the parameters.

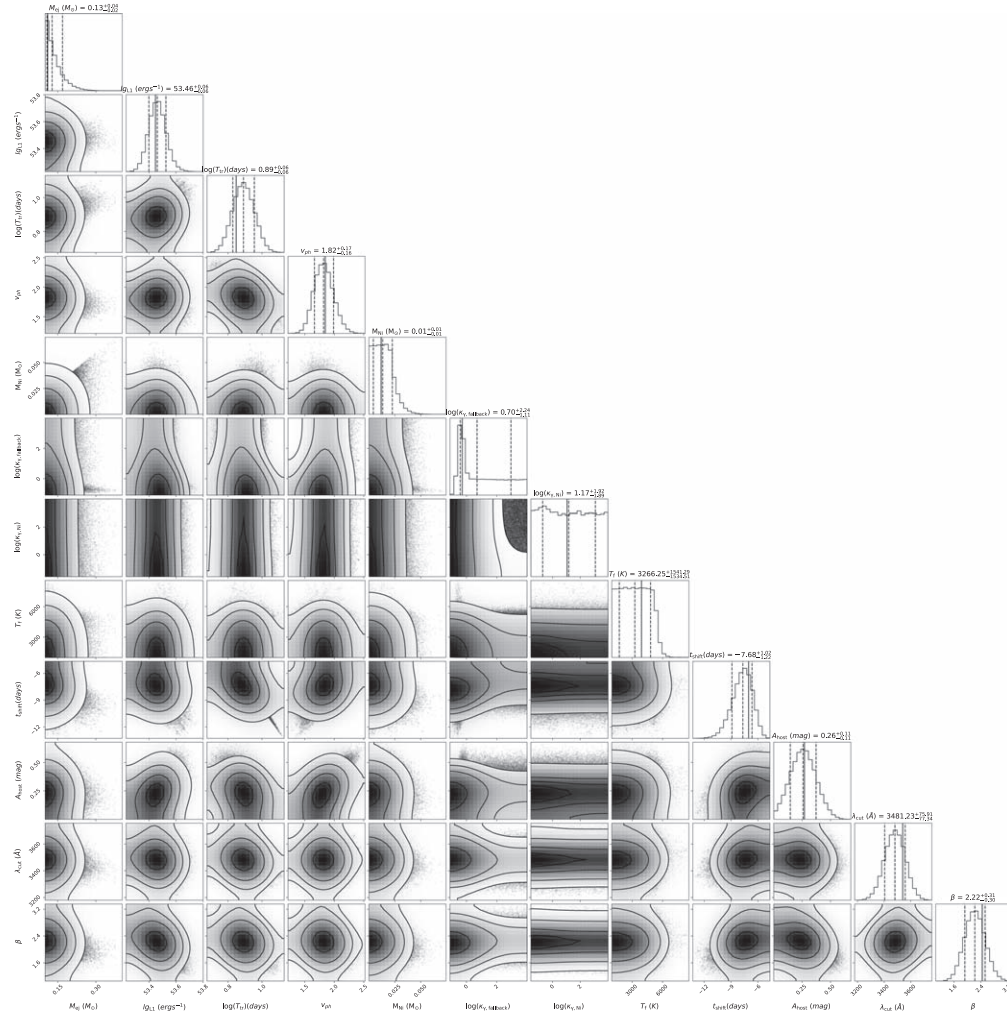


**Figure A10.** The corner plot of the fallback plus  $^{56}\text{Ni}$  model for the multi-band LCs of ASASSN-15mj. The solid vertical lines represent the best-fitting parameters, while the dashed vertical lines represent the medians and the  $1\sigma$  bounds of the parameters.

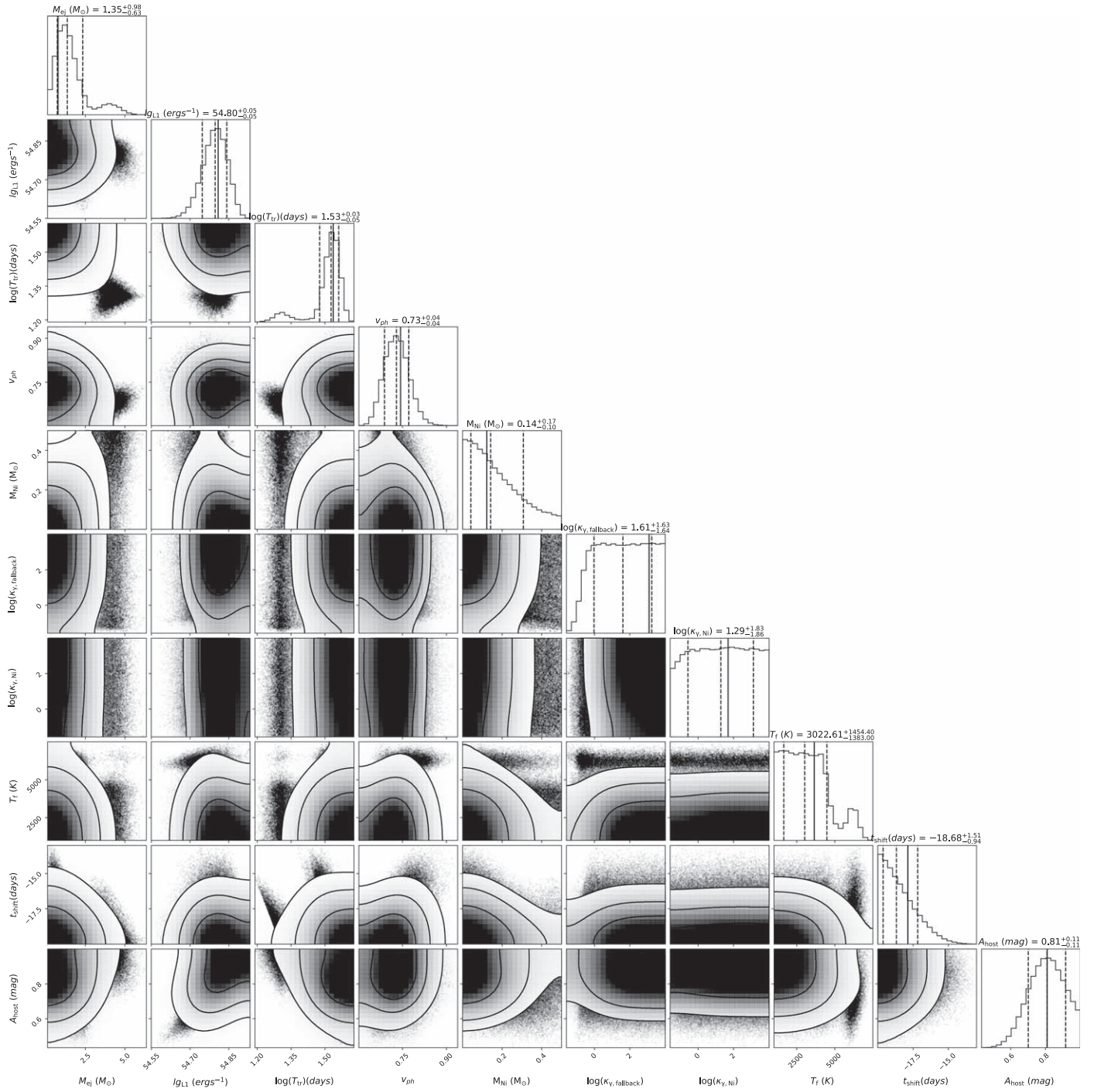


**Figure A11.** The corner plot of the fallback plus  $^{56}\text{Ni}$  model for the multi-band LCs of SN 2019omd. The solid vertical lines represent the best-fitting parameters, while the dashed vertical lines represent the medians and the  $1\sigma$  bounds of the parameters.

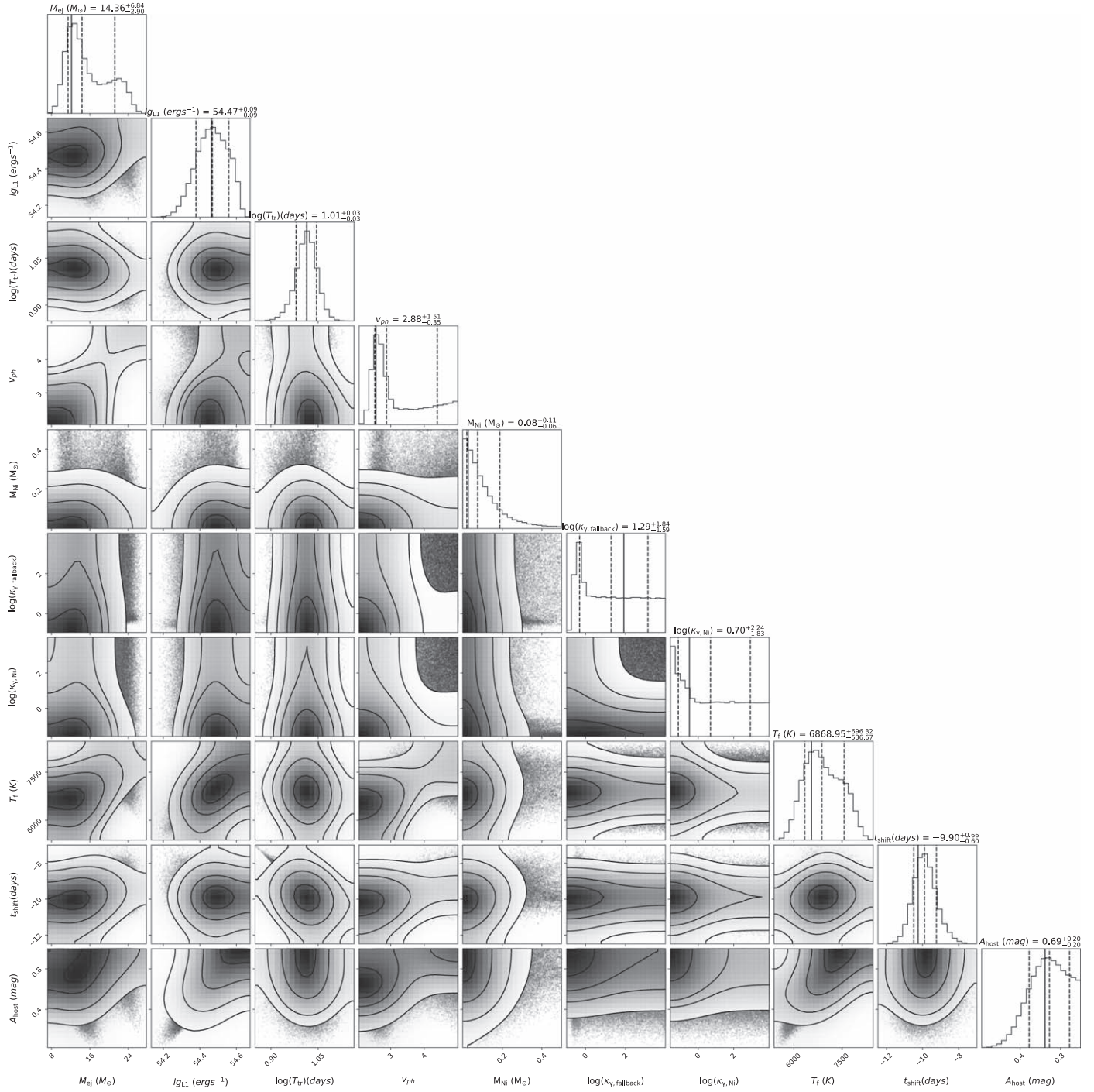


**Figure A12.** The corner plot of the fallback plus  $^{56}\text{Ni}$  model for the multi-band LCs of SN 2021bmf. The solid vertical lines represent the best-fitting parameters, while the dashed vertical lines represent the medians and the  $1\sigma$  bounds of the parameters.

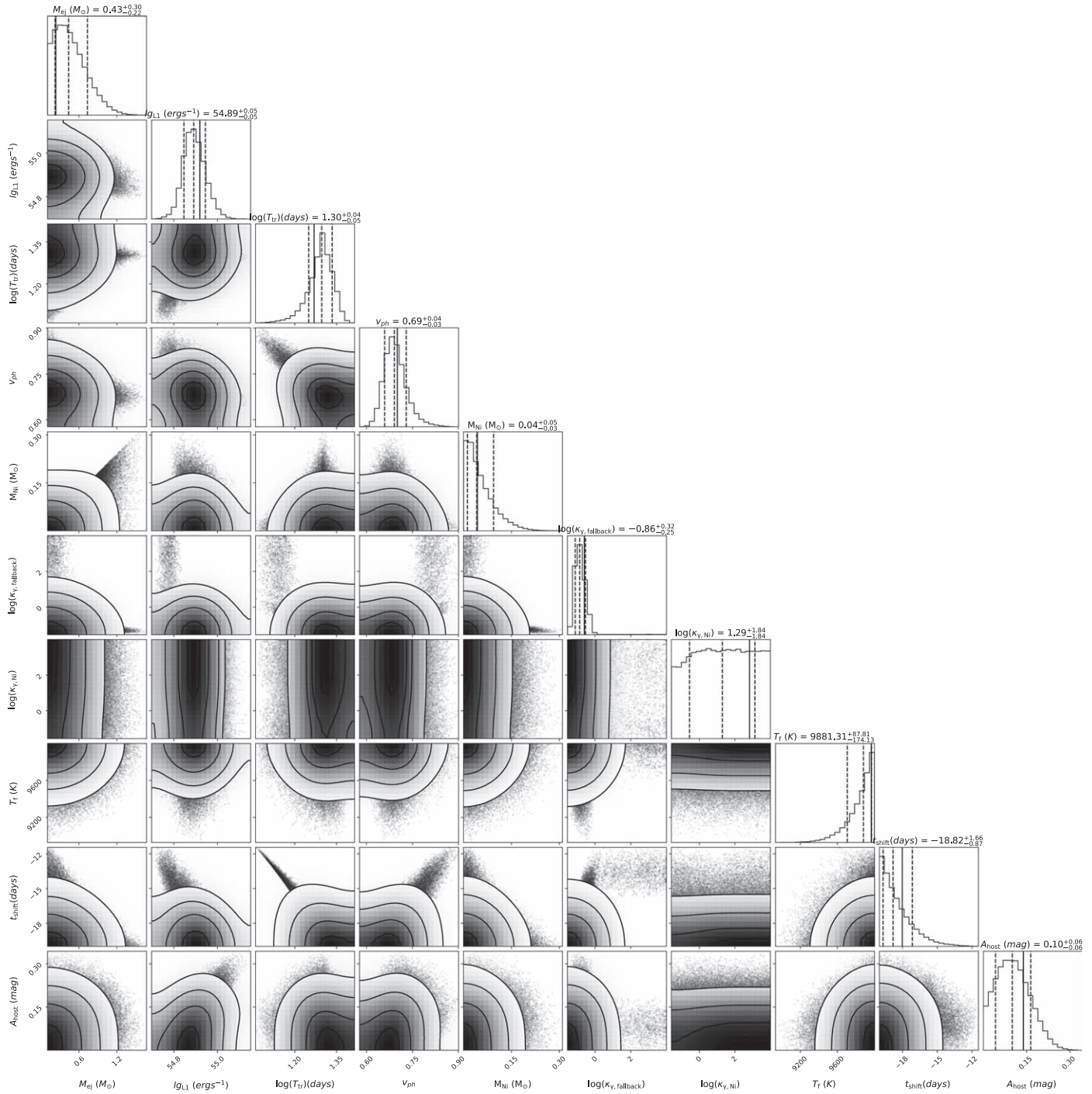


**Figure A13.** The corner plot of the fallback plus  $^{56}\text{Ni}$  model for the multi-band LCs of SN 2022ued. The solid vertical lines represent the best-fitting parameters, while the dashed vertical lines represent the medians and the  $1\sigma$  bounds of the parameters.

## References

Afsariardchi, N., Drout, M. R., Khatami, D. K., et al. 2021, *ApJ*, 918, 89  
 Anderson, J. P., Pessi, P. J., Dessart, L., et al. 2018, *A&A*, 620, A67  
 Arnett, W. D. 1982, *ApJ*, 253, 785

Blanchard, P. K., Berger, E., Nicholl, M., & Villar, V. A. 2020, *ApJ*, 897, 114  
 Chatzopoulos, E., Wheeler, J. C., & Vinko, J. 2012, *ApJ*, 746, 121  
 Chatzopoulos, E., Wheeler, J. C., Vinko, J., et al. 2013, *ApJ*, 773, 76  
 Chevalier, R. A. 1982, *ApJ*, 258, 790  
 Chevalier, R. A., & Fransson, C. 1994, *ApJ*, 420, 268

- Colgate, S. A., & McKee, C. 1969, *ApJ*, 157, 623
- Colgate, S. A., Petschek, A. G., & Kriese, J. T. 1980, *ApJL*, 237, L81
- Dexter, J., & Kasen, D. 2013, *ApJ*, 772, 30
- Filippenko, A. V. 1997, *ARA&A*, 35, 309
- Foreman-Mackey, D., Hogg, D. W., Lang, D., & Goodman, J. 2013, *PASP*, 125, 306
- Gal-Yam, A. 2012, *Science*, 337, 927
- Gal-Yam, A. 2017, *Handbook of Supernovae* (Berlin: Springer), 195
- Gal-Yam, A. 2019, *ARA&A*, 57, 305
- Gilkis, A., Soker, N., & Papish, O. 2016, *ApJ*, 826, 178
- Gomez, S., Berger, E., Hosseinzadeh, G., et al. 2021, *ApJ*, 913, 143
- Gomez, S., Berger, E., Nicholl, M., Blanchard, P. K., & Hosseinzadeh, G. 2022, *ApJ*, 941, 107
- Guillochon, J., Parrent, J., Kelley, L. Z., & Margutti, R. 2017, *ApJ*, 835, 64
- Insera, C., Smartt, S. J., Jerkstrand, A., et al. 2013, *ApJ*, 770, 128
- Janka, H.-T., Langanke, K., Marek, A., Martinez-Pinedo, G., & Müller, B. 2007, *PhR*, 442, 38
- Kasen, D., & Bildsten, L. 2010, *ApJ*, 717, 245
- Khatami, D. K., & Kasen, D. N. 2019, *ApJ*, 878, 56
- Kumar, P., Narayan, R., & Johnson, J. L. 2008, *MNRAS*, 388, 1729
- Li, L., Dai, Z. G., Wang, S. Q., & Zhong, S. Q. 2020, *ApJ*, 900, 121
- Maeda, K., Tanaka, M., Nomoto, K., et al. 2007, *ApJ*, 666, 1069
- McKinney, J. C. 2005, *ApJL*, 630, L5
- Moriya, T. J., Nicholl, M., & Guillochon, J. 2018a, *ApJ*, 867, 113
- Moriya, T. J., Terreran, G., & Blinnikov, S. I. 2018b, *MNRAS*, 475, L11
- Nicholl, M., Guillochon, J., & Berger, E. 2017, *ApJ*, 850, 55
- Perley, D. A., Fremling, C., Sollerman, J., et al. 2020, *ApJ*, 904, 35
- Prentice, S. J., Ashall, C., James, P. A., et al. 2019, *MNRAS*, 485, 1559
- Planck Collaboration, Ade, P. A. R., Aghanim, N., et al. 2014, *A&A*, 571, A16
- Richardson, D., Branch, D., Casebeer, D., et al. 2002, *AJ*, 123, 745
- Schlafly, E. F., & Finkbeiner, D. P. 2011, *ApJ*, 737, 103
- Shappee, B. J., Prieto, J. L., Grupe, D., et al. 2014, *ApJ*, 788, 48
- Stritzinger, M. D., Anderson, J. P., Contreras, C., et al. 2018, *A&A*, 609, A134
- Taddia, F., Stritzinger, M. D., Bersten, M., et al. 2018, *A&A*, 609, A136
- Umeda, H., & Nomoto, K. 2008, *ApJ*, 673, 1014
- Wang, S. Q., & Gan, W. P. 2022, *ApJ*, 928, 114
- Wang, S. Q., Wang, L. J., Dai, Z. G., et al. 2015a, *ApJ*, 799, 107
- Wang, S. Q., Wang, L. J., Dai, Z. G., & Wu, X. F. 2015b, *ApJ*, 807, 147
- Wang, T., Wang, S. Q., Gan, W. P., & Li, L. 2023, *ApJ*, 948, 138
- Whitesides, L., Lunnan, R., Kasliwal, M. M., et al. 2017, *ApJ*, 851, 107
- Woosley, S. E. 2010, *ApJL*, 719, L204
- Woosley, S. E., Heger, A., & Weaver, T. A. 2002, *RvMP*, 74, 1015